ACS OMEGA

http://pubs.acs.org/journal/acsodf

Article

Facile Synthesis of Polyindole/$Ni_{1-x}Zn_xFe_2O_4$ (x = 0, 0.5, 1) Nanocomposites and Their Enhanced Microwave Absorption and Shielding Properties

Anjitha Thadathil, Jithesh Kavil, Govind Raj Kovummal, Chamundi P. Jijil, and Pradeepan Periyat*

Cite This: *ACS Omega* 2022, 7, 11473−11490

Read Online

ACCESS | Metrics & More | Article Recommendations

ABSTRACT: The present work reports the fabrication of polyindole (PIN)/$Ni_{1-x}Zn_xFe_2O_4$ (x = 0, 0.5, 1) nanocomposites as efficient electromagnetic wave absorbers by a facile in situ emulsion polymerization method for the first time. The samples were characterized through Fourier transform infrared spectroscopy, UV−vis spectroscopy, X-ray diffraction, thermogravimetric analysis, scanning electron microscopy, high-resolution transmission electron microscopy, and vibrating sample magnetometry. The resulting polyindole/$Ni_{1-x}Zn_xFe_2O_4$ (x = 0, 0.5, 1) nanocomposites offer better synergism among the $Ni_{1-x}Zn_xFe_2O_4$ nanoparticles and PIN matrix, which significantly improved impedance matching. The best impedance matching of $Ni_{1-x}Zn_xFe_2O_4$/polyindole (x = 0, 0.5, 1) nanocomposites was sought out, and the minimum reflection loss of the composites can reach up to −33 dB. The magnetic behavior, complex permittivity, permeability, and microwave absorption properties of polyindole/$Ni_{1-x}Zn_xFe_2O_4$ (x = 0, 0.5, 1) nanocomposites have also been studied. The microwave absorbing characteristics of these composites were investigated in the 8−12 GHz range (X band) and explained based on eddy current, natural and exchange resonance, and dielectric relaxation processes. These results provided a new idea to upgrade the performance of conventional microwave-absorbing materials based on polyindole in the future.

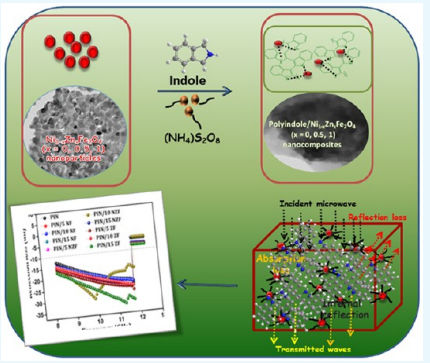

INTRODUCTION

The development of high-performance electromagnetic interference (EMI) shielding/microwave-absorbing materials has become a current focus in solving the problem of EMI pollution arising from the fast-growing telecommunication equipment and other electro-electronic device industries.[1,2] In the last decade, the charm of 2D nanomaterials, such as graphene,[3,4] g-C_3N_4,[5] MXenes,[6] WS_2,[7] and MoS_2,[8] has intrigued great deal of interest due to their microwave-absorbing properties originating from their broadband optical response, strong plasmon oscillation, gate-tunable conductivity, active variable THz band gaps, and enormous surface area-to-volume ratio. In addition, as a new class of Dirac materials with a small band gap, TI was also found to show saturable absorption at telecommunication wavelengths.[9] In general, it is noticed that individual magnetic and dielectric electromagnetic wave-absorbing materials show satisfactory performance due to the poor impedance matching.[10] Accordingly, noteworthy attempts have been made to build high-performance composite microwave-absorbing materials comprising both magnetic and dielectric components, which would offer better impedance matching and improved electromagnetic shielding performance through the effective complementarities and synergies between magnetic loss and dielectric loss.[11,12] Recently, researchers have explored the effect of nanoparticle-induced moderations in conducting polymers that possess the most effective colligative electronic, magnetic, and optical properties. Conducting polymer ferrite composites have drawn much attention as an EMI-shielding/absorbing material due to their high dielectric and magnetic losses,[13] corrosion resistance, low density, and ease of processing.[14] Among the conducting polymers, polyindole (PIN) and its derivatives have not yet been explored as microwave-absorbing/shielding materials. Despite several advantages such as air-stable electrical conductance,[15] slow hydrolytic degradation,[16] high redox activity,[17] high cycling, and thermal stability as compared to polyaniline (PANI) and polypyrrole (PPY), PIN still suffers from lesser conductivity than PANI and PPY.[18] However, electrical conductivity in the range from 10^{-3} to 10^{-1} S cm^{-1} is shown by PIN in its doped state.[19,20] When organic dopants with surfactant functionalities such as sodium dodecyl sulfate (SDS) and sodium dodecylbenzenesulfonate (SDBS) are employed, they play a dual role as dopants and as a

Received: February 10, 2022
Accepted: March 15, 2022
Published: March 24, 2022

surfactant[13,20,21] and improve the conductivity of PIN. It has been reported that such synthetic conductive polymers including PPY, PANI, PTh, and PIN reinforce the polarizability, conductance, and impedance matching of the absorbers, realizing more microwave attenuation.[22] More significantly, the salient potential of the conductive polymers in anticorrosive coatings,[23] energy storage, electrochemical supercapacitors,[24] sensing,[25] environmental remediation,[26] antimicrobial properties, water treatment,[27] and energy recovery fields has boosted their significance.

In recent years, researchers have had a great interest in spinel ferrite nanoparticles due to their extensive applications in gas sensing,[28] inductors,[29] biosensing,[30] sequestration of lanthanides and actinides from aqueous solutions,[31] telecommunications,[32] and hyperthermia applications in cancer therapy.[33] Magnetic nanoparticles such as Fe_3O_4,[34−36] $ZnFe_2O_4$,[36,37] $NiFe_2O_4$,[38−40] and $(NiZn)Fe_2O_4$[41,42] are well-known traditional microwave absorbers, proven to have significant magnetic loss properties. Due to their low eddy current losses, they show wide electronic applications in terms of power generation, conditioning, and conversion.[43] These properties also endow them a unique value in microwave devices including microwave nonreciprocal passive devices, microwave signal-processing devices, negative index metamaterial-based electronics, and in EMI suppression that require strong coupling to electromagnetic signals and often nonreciprocal behavior.[44] The electromagnetic wave absorption properties of conducting polymers can be improved by compositing them with magnetic materials.[34] Yang and coworkers[45] fabricated Fe_3O_4−hollow PANI composites and found that the composites could produce much better microwave absorption (MA) characteristics than sole PANI microspheres. Gandhi et al.[46] reported a ferromagnetic polyaniline−$CoFe_2O_4$ nanocomposite with enhanced EMI shielding effectiveness (SE) in the frequency range of 12.4−18.0 GHz (Ku band). Li et al.[47] presented a comparison of MA properties of composites of $NiFe_2O_4$ with PANI and PPY, respectively, and revealed that the $NiFe_2O_4$/PPY composite would be an eligible candidate for EMI shielding.

In this study, the impact of Zn^{2+} substitution in $NiFe_2O_4$ spinel ferrite nanoparticles on their structural and magnetic properties was investigated. Moreover, the impact of Zn^{2+} substitution in $NiFe_2O_4$ spinel ferrite nanoparticles on the microwave absorbing and shielding properties of their nanocomposites with PIN as matrix polymer was investigated. An intrinsically conducting polymer, PIN, was utilized as a polymer matrix because of its corrosion resistance property, lightweight, desirable electrical conductivity, ease of synthesis, low cost, and capability of interacting with EM radiation through both absorption and reflection mechanisms over a wide range of frequencies. However, due to the nonmagnetic characteristic of PIN, it can only provide dielectric loss and conducting characteristics, thus resulting in impedance mismatching issues. The combination of PIN with magnetic spinel ferrite nanoparticles can balance impedance matching conditions. Spinel ferrites $NiFe_2O_4$ (NF), $Ni_{0.5}Zn_{0.5}Fe_2O_4$ (NZF), and $ZnFe_2O_4$ (ZF) are best known for their low dielectric loss, large permeability, high magnetic loss properties, high electric resistivity, and unique magnetic structure. The substitution of Zn^{2+} with diamagnetic characteristics in $NiFe_2O_4$ spinel ferrite can induce modifications in the structural and electromagnetic properties associated with the distribution of cations at octahedral and tetrahedral sites. In principle, the combination of high-permeability materials having significant magnetic loss properties and high-permittivity materials with dielectric loss properties enables the design of efficient microwave-shielding materials. The interface introduced by $Ni_{1-x}Zn_xFe_2O_4$ (x = 0, 0.5, 1) ferrite nanoparticles generates resonance in complex permittivity and permeability, as well as enhanced magnetic loss, which results in the enhanced MA and widened effective absorption bandwidth. Hence, a unique combination of a conducting PIN matrix with $Ni_{1-x}Zn_xFe_2O_4$ (x = 0, 0.5, 1) ferrite nanoparticles can balance impedance matching conditions and offer an effective way to design high-performance functional materials to facilitate research in electromagnetic shielding and MA. Here, we synthesized nanocomposites of $ZnFe_2O_4$ (ZF), $NiFe_2O_4$ (NF), and $Ni_{0.5}Zn_{0.5}Fe_2O_4$ (NZF) with PIN via the in situ emulsion polymerization method using SDBS and well characterized with Fourier transform infrared (FTIR) spectroscopy, UV−vis spectroscopy, X-ray diffraction (XRD), scanning electron microscopy (SEM), high-resolution transmission electron microscopy (HRTEM), and vibrating sample magnetometry (VSM). The magnetic properties, complex permittivity, permeability, and MA properties of PIN/$Ni_{1-x}Zn_xFe_2O_4$ (x = 0, 0.5, 1) nanocomposites have been investigated and compared with the pristine PIN. To the best of our knowledge, this is the first detailed study on PIN-based nanocomposites with Zn^{2+}-doped $NiFe_2O_4$ nanoparticles for microwave absorbing and shielding applications. The present work provides methods for the development of high-performance nanocomposites based on PIN as potential candidates for EMI absorption and shielding application.

EXPERIMENTAL SECTION

Materials. Iron nitrate [$Fe(NO_3)_3{\cdot}9H_2O$], zinc nitrate [$Zn(NO_3)_2{\cdot}6H_2O$], and nickel nitrate $Ni(NO_3)_2{\cdot}6H_2O$) with 99% of purity were purchased from Sigma-Aldrich. Indole powder (monomer), ammonium persulfate $(NH_4)_2S_2O_8$ (APS), SDBS, and citric acid were procured from HiMedia, India. Deionized water and ethanol were used as the solvents for the synthesis.

Synthesis of PIN. PIN was prepared by a simple chemical oxidative emulsion polymerization of indole using ammonium persulfate (APS) as an oxidizing agent.[20] For the synthesis, 1.18 g of SDBS was dissolved in 0.1 M HCl (180 mL) and a homogeneous surfactant solution was prepared by continuously stirring it at room temperature. Subsequently, 2 g of indole was dissolved in 10 mL of ethanol, which was gradually added into the mixture solution and sonicated for 1 h. Finally, 1.16 g of APS in 0.1 M HCl was added dropwise and the solution turned dark green in color. The ratio of indole to APS was fixed at 1:1.25. After that, the mixture solution was continuously stirred for 24 h. The precipitate was rinsed with 1 M HCl (200 mL) and washed with distilled water several times before drying in an oven at 70 °C overnight to obtain PIN powder. The dried PIN precipitate was ground and stored in a desiccator overnight until further use.

Synthesis of $Ni_{1-x}Zn_xFe_2O_4$ (x = 0, 0.5, 1) Nanoparticles. The nanoparticles of $Ni_{1-x}Zn_xFe_2O_4$ (x = 0, 0.5, 1) were synthesized by the sol−gel autocombustion method.[48] For the synthesis of $ZnFe_2O_4$ (x = 1) (ZF) nanoparticles, iron nitrate (1.0 M) and zinc nitrate (0.5 M) (2:1 molar ratio) solutions were mixed thoroughly with 2.2 M citric acid (1:2.22 molar ratio with nitrates) to get a clear solution. A small amount of ammonia was added carefully to the solution to

https://doi.org/10.1021/acsomega.2c00824
ACS Omega 2022, 7, 11473−11490

Scheme 1. Schematic Representation of In Situ Emulsion Polymerization of the PIN/$Ni_{1-x}Zn_xFe_2O_4$ (x = 0, 0.5, 1) Nanocomposite Using APS as an Oxidant

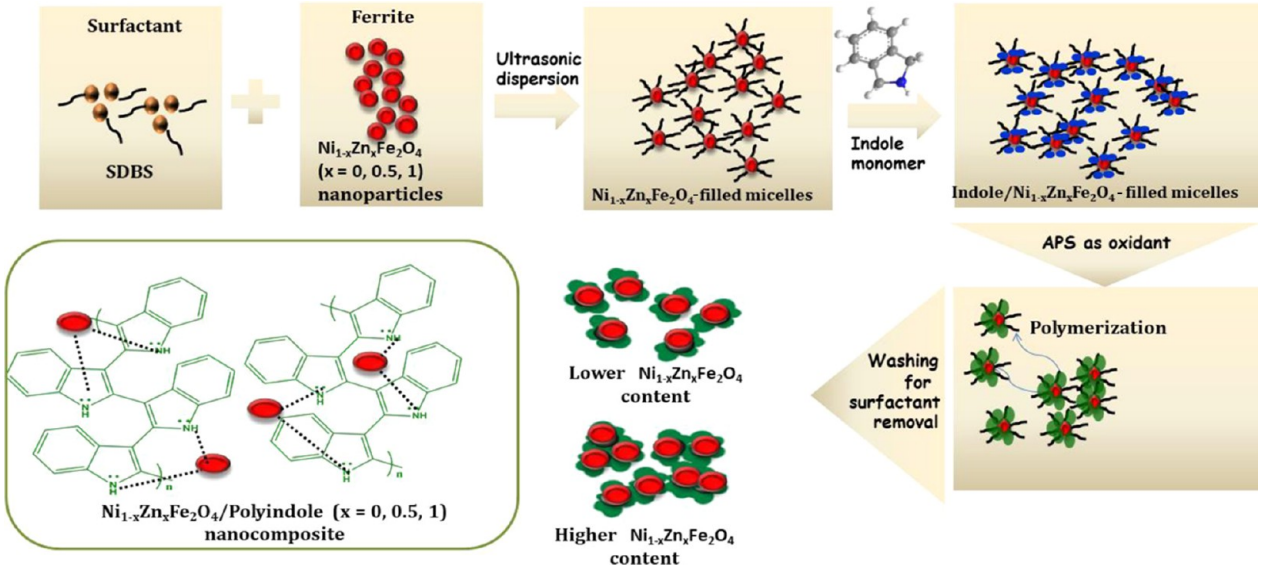

adjust the pH value to 7. During this procedure, the solution was continuously stirred using a magnetic stirrer and maintained at a temperature of 90 °C until the gel formed. Then, it was heated to 150 °C, which led to the formation of nanopowders through a self-propagating combustion process. The loose powder was crushed well and calcined at 550 °C for 4 h to form the spinal phase. A similar procedure was followed for the synthesis of $NiFe_2O_4$ (NF) and $Ni_{0.5}Zn_{0.5}Fe_2O_4$ (NZF) nanoparticles (x = 0 and 0.5, respectively). In the synthesis of NZF nanoparticles, the molar ratio of metal nitrates was fixed at Ni/Zn/Fe = 1:1:4, whereas the molar ratio of nitrates to citric acid was 1:2.77. For NF nanoparticle synthesis, iron nitrate (1.0 M) and nickel nitrate (0.5 M) (2:1 molar ratio) solution were mixed with 2.2 M citric acid (1:2.22 molar ratio with nitrates).

Synthesis of PIN/$Ni_{1-x}Zn_xFe_2O_4$ (x = 0, 0.5, 1) Nanocomposites. PIN/$Ni_{1-x}Zn_xFe_2O_4$ (x = 0, 0.5, 1) nanocomposites were synthesized by the in situ emulsion polymerization of indole in an aqueous solution containing the ferrite nanofluid using APS as the oxidizing agent.[17] Then, 5, 10, and 15 wt % of NF, NZF, and ZF nanoparticles were mixed, respectively, with SDBS in 10 mL of water and ultrasonicated for 10 min. Subsequently, 3 g of indole in 10 mL of ethanol was mixed with 0.293 g of SDBS in 50 mL of 0.1 M of HCl and gradually added into the mixture solution. This solution was ultrasonicated for 1 h. Finally, 1.75 g of APS in 0.1 M HCl was added dropwise and the solution turned dark green in color. The polymerization reaction was carried out for 24 h with continuous magnetic stirring. The precipitate finally obtained was rinsed with 1 M HCl (200 mL) and washed with distilled water several times before drying in an oven at 70 °C overnight to obtain nanocomposites with different wt % of NF, NZF, and ZF nanoparticles in the PIN matrix. The sample code is given as PIN/5 NF, PIN/10 NF, PIN/15 NF, PIN/5 NZF, PIN/10 NZF, PIN/15 NZF, PIN/5 ZF, PIN/10 ZF, and PIN/15 ZF. The dried composites were then pressed into rectangular pellets having dimensions of 22.86 × 10.16 mm for X-band measurements.

Characterizations. The chemical structure of the samples was analyzed using a JASCO (model 4100) FTIR spectrophotometer in the region of 4000−350 cm^{-1} by the KBr pellet method. UV−vis diffuse reflection spectroscopy (UV−vis DRS) was conducted using a UV−vis−NIR spectrophotometer (JASCO V-550). Phase identification and the study of the morphology of PIN and its composites were carried using a powder X-ray diffractometer [X'Pert^3 powder with Cu Kα (λ = 1.5406 Å) radiation]. Thermogravimetric analysis (TGA) was performed using a STA 8000 TG-DTA analyzer. The morphology of the sample was measured using a scanning electron microscope (Hitachi S-3000H) and transmission electron microscope (JEOL/JEM2100 with a 200 kV accelerating voltage and a lattice resolution of 0.14 nm). Magnetic measurements were performed using a Quantum Design MPMS 7T SQUID VSM system. The EMI SE values in the X (8.2−12.4 GHz) band region were calculated from the reflection (S_{11} and S_{22}) and transmission (S_{21} and S_{21}) scattering parameters measured using a vector network analyzer (Agilent E5071C) using the waveguide method.

RESULTS AND DISCUSSION

The formation of PIN/$Ni_{1-x}Zn_xFe_2O_4$ (x = 0, 0.5, 1) composites has been carried out via a simple and facile in situ emulsion polymerization method, in which the indole solution is emulsified with the surfactant SDBS containing $Ni_{1-x}Zn_xFe_2O_4$ (x = 0, 0.5, 1) nanoparticles, in a continuous phase of water. In emulsion polymerization, the surfactant has dual functions as a template and codopant.[20] When the surfactants act as a template, the reaction takes place in the nanoreactor of surfactant micelles, whereas in the role of a dopant, ionic complex formation organizes the polymer backbone.[49] Above the critical micelle concentration (CMC), surfactants can form micelles, where the hydrophilic "head" regions are in contact with the solvent, sequestering the hydrophobic tail regions in the micelle center. When an indole solution is added to the surfactant solution with ferrite nanoparticles, it diffuses through the water to the micelles. The presence of the oxidant APS in the solution leads to oxidative polymerization, where indole is oxidized. The fabrication of PIN/$Ni_{1-x}Zn_xFe_2O_4$ (x = 0, 0.5, 1) composites *via* an in situ emulsion polymerization method is presented in Scheme 1.

https://doi.org/10.1021/acsomega.2c00824
ACS Omega 2022, 7, 11473−11490

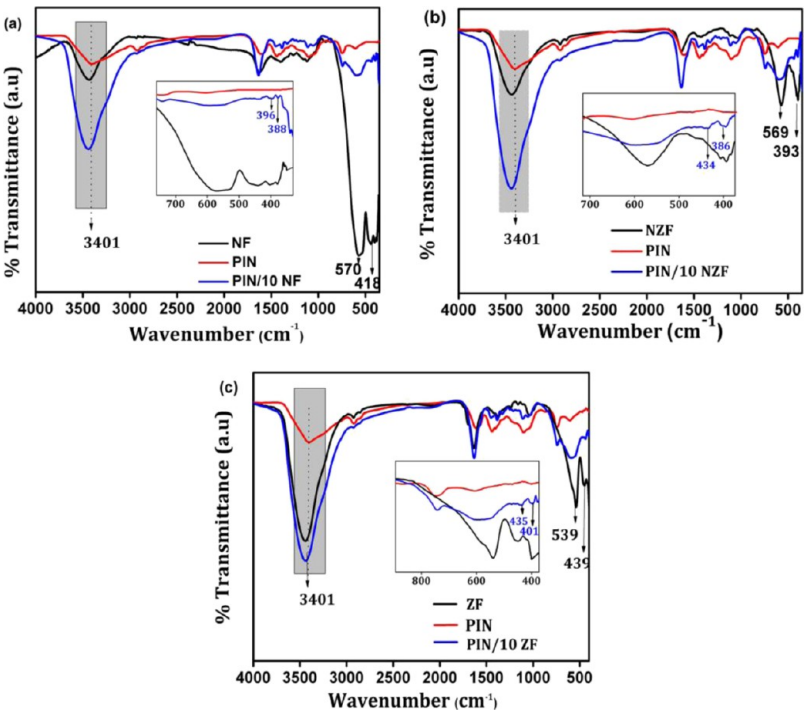

Figure 1. Comparison of FTIR spectra of (a) PIN, NF, and PIN/10 NF, (b) PIN, NZF, and PIN/10 NZF, and (c) PIN, ZF, and PIN/10 ZF.

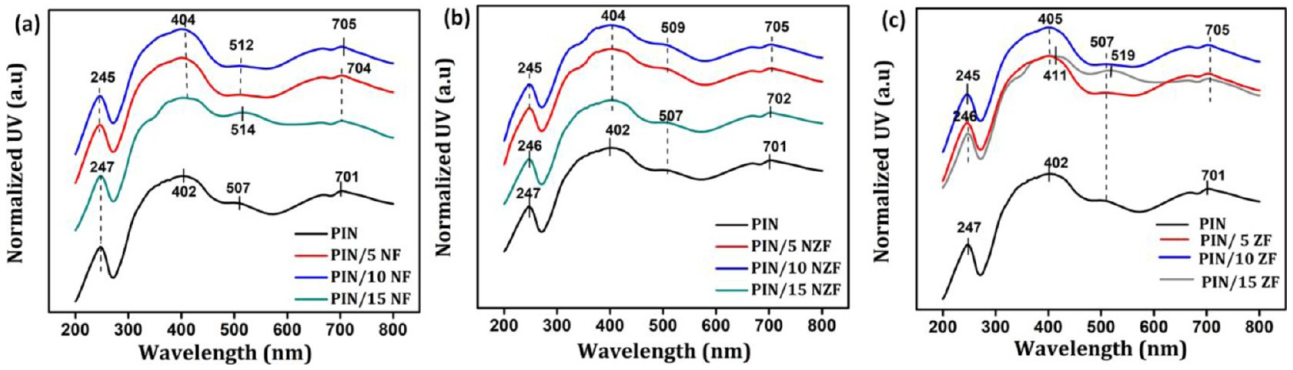

Figure 2. Normalized UV−vis DRS spectra of (a) PIN and PIN/NF, (b) PIN and PIN/NZF, and (c) PIN and PIN/ZF powder composites with 5, 10, and 15 wt % ferrite ratios.

FTIR Spectroscopy Analysis. Figure 1a−c shows the FTIR spectra of PIN and its nanocomposites with NF, ZF, and NZF nanoparticles in the range of 4000−350 cm^{-1}. The characteristic bands in the IR spectrum of PIN occur at 3401, 1380, 1442, 1594, 1191, and 750 cm^{-1}. The band at 3401 cm^{-1} is ascribed to the characteristic N−H stretching vibrations in PIN. The presence of this band proved that the nitrogen atom of indole is not involved in polymerization.[17] The bands at 1442 and 1594 cm^{-1} are due to the C−C stretching vibration mode of the benzene ring in PIN.[50] The band at 750 cm^{-1} is due to the characteristic out-of-plane deformation of the C−H bond in the benzene ring,[51] and the absorption at 1191 cm^{-1} is assigned to the in-plane C−H bending modes present in the aromatic heterocyclic part of indole. The prominent sharp and intense spectral band at 1380 cm^{-1} is due to the vibration mode of the C−N bond in PIN.[50] In spinel ferrites, metal ions are usually situated at two different sublattices designated as tetrahedral and octahedral sites according to the geometrical configuration of the oxygen nearest neighbor.[52] It is evident in Figure 1 that NF, NZF, and ZF nanoparticles displayed their fingerprint peaks at around 350−590 cm^{-1}, which is ascribed to the stretching vibration of metal−oxygen bonds in tetrahedral and octahedral sites.[53] The ZF nanoparticles offered the Zn^{2+}−O^{2-} tetrahedral stretching frequency at 435 cm^{-1} and the Fe^{3+}−O^{2-} octahedral stretching frequency at 401 cm^{-1}. For the NZF and NF nanoparticles, the Ni^{2+}−O^{2-} octahedral stretching peaks appeared at 386 and 388 cm^{-1}, respectively (inset of Figure 1). The presence of Fe^{3+}−oxygen complexes in the octahedral site causes the splitting of absorption bands due to local lattice deformation.[54] The spectra of NF, NZF, and ZF show prominent bands near 3400 and 1600 cm^{-1}, which are attributed to the stretching modes and H−O−H bending vibrations of free or absorbed water, respectively.[55]

The interaction of ferrite nanoparticles with the PIN matrix can be visible from the IR data of their respective nanocomposites depicted in Figure 1, which exhibit characteristic peaks of both PIN and ferrite nanoparticles. Close scrutiny of the spectra of the nanocomposites indicates that the characteristic peaks of ferrite nanoparticles shifted to lower

https://doi.org/10.1021/acsomega.2c00824
ACS Omega 2022, 7, 11473−11490

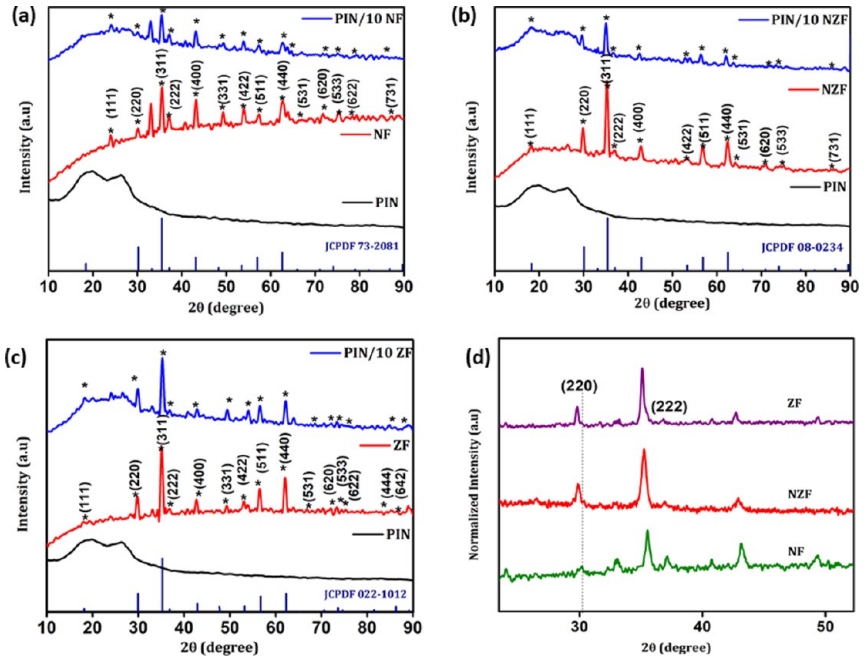

Figure 3. XRD patterns of (a) PIN, NF, and PIN/10 NF, (b) PIN, NZF, and PIN/10 NZF, (c) PIN, ZF, and PIN/10 ZF, and (d) enlarged view of the XRD patterns of NF, NZF, and ZF.

wavenumbers and the intensity of the peaks greatly diminished. These observations confirm that there is a good wrapping of ferrite nanoparticles within PIN in the nanocomposites. Furthermore, the N−H absorption band of the composite is found to shift to a higher wavenumber from 3401 cm^{-1}, showing that the N−H group of PIN interacts with the metal ions of ferrite nanoparticles.

UV−Vis Spectral Analysis. UV−visible spectroscopy has been used to characterize the interfacial interaction between PIN and ferrite nanoparticles in the nanocomposites. The UV−vis DRS absorption spectra of the powdered samples of pristine PIN and PIN/$Ni_{1-x}Zn_xFe_2O_4$ (x = 0, 0.5, 1) nanocomposites normalized with respect to the amount of PIN are shown in Figure 2. The UV−vis DRS spectra of PIN show four characteristic bands in the entire region of UV−vis spectra. The sharp peak positioned at 247 nm originates due to $\pi-\pi^*$ transitions in the polymer chain.[6] The broad peak at 402 nm is related to the n−π^* transitions, while the bands at about 507 and 701 nm represent the polaron to π^* band transition and the π to polaron band transition of the PIN chains, respectively.[56] As shown in Figure 2, the insertion of ferrite nanoparticles affects the position and intensity of UV peaks in the PIN nanocomposites. As the ferrite content increases in different samples, $\pi-\pi^*$ transitions in the absorption spectra show a hypsochromic shift from 247 to 245 nm. It is also interesting to note that the n−π^* transition at 402 nm of PIN shows a red shift to 404−411 nm in the PIN/$Ni_{1-x}Zn_xFe_2O_4$ (x = 0, 0.5, 1) nanocomposites. The reason behind this shifting may be the possible interaction of the ferrite nanoparticles with the PIN ring, leading to the formation of a ferro-/ferrimagnetic nanocomposite. Also, it is important to observe that the polaron to π^* band transition and π band to polaron band transition of PIN exhibits a red shift from 507 to 519 and 701 to 705 nm, respectively, in the PIN/$Ni_{1-x}Zn_xFe_2O_4$ (x = 0, 0.5, 1) nanocomposites, indicating that the band gap of such transition becomes progressively lower in the nanocomposites. It is evident from the figure that the intensity of the absorption edge is found to decrease as the content becomes 15 wt %. This result indicates the aggregation of nanofillers at a higher loading, which resists the absorption of incident light.[31]

XRD Analysis. The crystal structures of PIN, NF, NZF, and ZF nanoparticles and their nanocomposites with PIN are characterized by XRD, as presented in Figure 3. In the XRD patterns, PIN shows broad peaks at 18.8 and 27.2°. The presence of these broad peaks confirms the polymerization of indole, and the diffraction peak at 27.2° validates the partial crystalline nature of PIN.[17] As can be seen in Figure 3, the existence of the (220), (311), (400), (422), (511), and (440) major lattice planes in the XRD patterns of ferrite nanoparticles confirms the formation of a spinel cubic structure with the *Fd*3*m* space group. Also, the presence of the (111), (222), (331), (533), and (622) minor lattice planes in the XRD patterns agrees well with the powder diffraction of the spinel cubic phase. The characteristic diffraction peaks are in good agreement with JCPDS-00-73-2081, JCPDS-00-008-0234, and JCPDS-00-022-1012 for NF, NZF, and ZF nanoparticles, respectively. The literature reveals that the intensities of the (220) and (222) planes are sensitive to cations on the tetrahedral and octahedral sites.[57] Figure 3d clearly shows the shift of the (220) peak toward a lower diffraction angle and a rise in the I_{220}/I_{222} ratio as the zinc content (x) increases, which implies that Zn^{2+} ions have preferentially occupied the A sites following the replacement of Ni^{2+} by Zn^{2+} ions. At about 35°, a diffraction peak with a relatively wide full width at half-maximum (fwhm) is measured in the XRD curve of ferrite nanoparticles. From this data, the average crystallite size of ferrite nanoparticles is calculated using the Scherrer eq 1

$$D = \frac{K\lambda}{\beta \cos\theta} \tag{1}$$

where k is a constant (0.94), λ is the wavelength of X-rays (0.154 nm), β is the corrected fwhm of the strongest diffraction peak in radians, and θ is the diffraction angle. The average crystallite size of the NF, NZF, and ZF nanoparticles

https://doi.org/10.1021/acsomega.2c00824
ACS Omega 2022, 7, 11473−11490

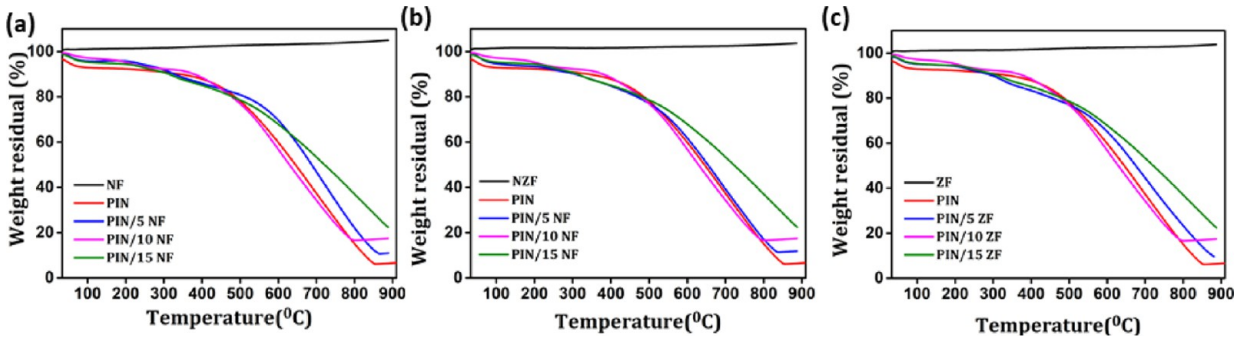

Figure 4. TG curves of (a) PIN, NF, and PIN/NF, (b) PIN, NZF, and PIN/NZF, and (c) PIN, ZF, and, PIN/ZF powder composites with 5, 10, and 15 wt % ferrite ratios.

was found to be 7.5, 9.6, and 23.3 nm, respectively. Interestingly, the crystallite size slightly increases when more Ni^{2+} ions are replaced with Zn^{2+} ions in the NZF nanoparticles. This is due to the larger size of the Zn^{2+} ions (0.83 Å) compared to the Ni^{2+} ions (0.78 Å).[48] However, the exceptionally high crystalline size of ZF nanoparticles is attributed to the sample's tendency to fuse at high temperatures and can be explained by an aggregative growth mechanism.[58,59] As shown in Figure 3, it is seen that both the characteristic amorphous peaks of PIN and the signature peaks for pristine ferrite nanoparticles appear in the diffraction patterns of PIN/$Ni_{1-x}Zn_xFe_2O_4$ (x = 0, 0.5, 1) nanocomposites. This suggests that nanoparticles have been successfully incorporated into the PIN matrix.

It is also evident that the intensities of the signature peaks for ferrite nanoparticles become weaker in the PIN/$Ni_{1-x}Zn_xFe_2O_4$ (x = 0, 0.5, 1) nanocomposites, compared to pure ferrite nanoparticles, which is on account of the PIN coating on the surface of nanoparticles.

Thermal Analysis. The TGA curves of pure PIN, $Ni_{1-x}Zn_xFe_2O_4$ (x = 0, 0.5, 1), and nanocomposites with different $Ni_{1-x}Zn_xFe_2O_4$ (x = 0, 0.5, 1) loadings, exhibited in Figure 4, are exploited to study their thermal stability. In Figure 4, it is found that the mass of NF, NZF, and ZF nanoparticles has a less loss of about 0.01% in the whole course upon increasing the temperature. It is observed that there are two-stage degradations in the pure PIN and its nanocomposites. In the first stage (30−95 °C), the weight loss of the samples is caused by the evaporation of moisture and dopant in the polymer,[60] whereas the second stage (350−850 °C), major weight loss, results from the thermal degradation of the PIN polymer chain.[61] At 850 °C, PIN retains only 6.4% of the initial weight, which reveals high thermal degradability of the PIN backbones. The weight residual of the nanocomposites with $Ni_{1-x}Zn_xFe_2O_4$ (x = 0, 0.5, 1) with loadings of 5, 10, and 15 wt % are shown in Table 1. The small divergence between the weight residues calculated from the TGA curves and the initial loading calculated by the indole monomers and $Ni_{1-x}Zn_xFe_2O_4$ (x = 0, 0.5, 1) nanoparticles in the fabrication may be a result of the incomplete reaction of indole monomers during polymerization.

Microstructure Studies. Figure 5 shows the FESEM micrographs of PIN, NF, NZF, and ZF nanoparticles and their composites with PIN at 10 wt % filler ratios. Agglomerated uniform nanometric particles of NF, NZF, and ZF with the average particle size in the range of 5−35 nm can be observed in Figure 5. As it is seen, the agglomerate's size decreases and the particles dispersed are more homogeneous in the PIN/

Table 1. Thermal Properties of Pure PIN, NF, NZF, ZF, and PIN/$Ni_{1-x}Zn_xFe_2O_4$ (x = 0, 0.5, 1) Nanocomposites

samples	weight residue (wt %) at 880 °C	wt % $Ni_{1-x}Zn_xFe_2O_4$ (x = 0, 0.5, 1) in the PIN/Ni_{1-x}ZnxFe2O4 (x = 0, 0.5, 1) nanocomposites
PIN	6.4	
NF	99.99	
NZF	99.99	
ZF	99.99	
PIN/5NF	11.5	5.1
PIN/10NF	17.2	10.8
PIN/15NF	22.1	15.7
PIN/5NZF	11.8	5.4
PIN/10NZF	16.9	10.5
PIN/15NZF	22.3	15.9
PIN/5ZF	11.1	4.7
PIN/10ZF	16.8	10.4
PIN/15ZF	23.2	16.8

10$Ni_{1-x}Zn_xFe_2O_4$ (x = 0, 0.5, 1) nanocomposites. The PIN layers may have wrapped on the surface of the $Ni_{1-x}Zn_xFe_2O_4$ (x = 0, 0.5, 1) nanoparticles, forming these agglomerated globules with a smooth surface in the PIN/10$Ni_{1-x}Zn_xFe_2O_4$ (x = 0, 0.5, 1) nanocomposites. That is to say, the irregular surface morphology of the nanoparticle changes into spherically shaped particles by the in situ polymerization of indole with ferrite nanoparticles. Further structural characterization using TEM was carried out to provide a visual demonstration of the structure and to estimate the grain size exactly.[62] The representative TEM micrographs of nanocrystalline NF, NZF, and ZF nanoparticles and PIN/10$Ni_{1-x}Zn_xFe_2O_4$ (x = 0, 0.5, 1) nanocomposites at low and high resolutions are presented in Figure 6. According to Figure 6a−c, the nanoparticles are roughly spherical, and the average particle size is determined from the log-normal fitting of the particle size distribution graph. The insets in the TEM micrographs at low magnifications present the histogram by counting 200 nanoparticles. It is found that the average particle sizes of NF, NZF, and ZF are obtained as 8, 14.49, and 34.09 nm, respectively. It is also noted that the particle size of NF, NZF, and ZF nanoparticles determined from TEM is higher than the crystalline size obtained from XRD. This result confirms that one particle can be constituted by several crystalline domains.

In Figure 6d−f, the atomic lattice fringes can be observed and the interplanar spacings were measured to be 4.8, 2.9, and 2.5 Å, which were close to the {111}, {220}, and {311} lattice planes of cubic $Ni_{1-x}Zn_xFe_2O_4$ (x = 0, 0.5, 1) respectively. The selected-area electron diffraction (SAED) pattern of a single

https://doi.org/10.1021/acsomega.2c00824
ACS Omega 2022, 7, 11473−11490

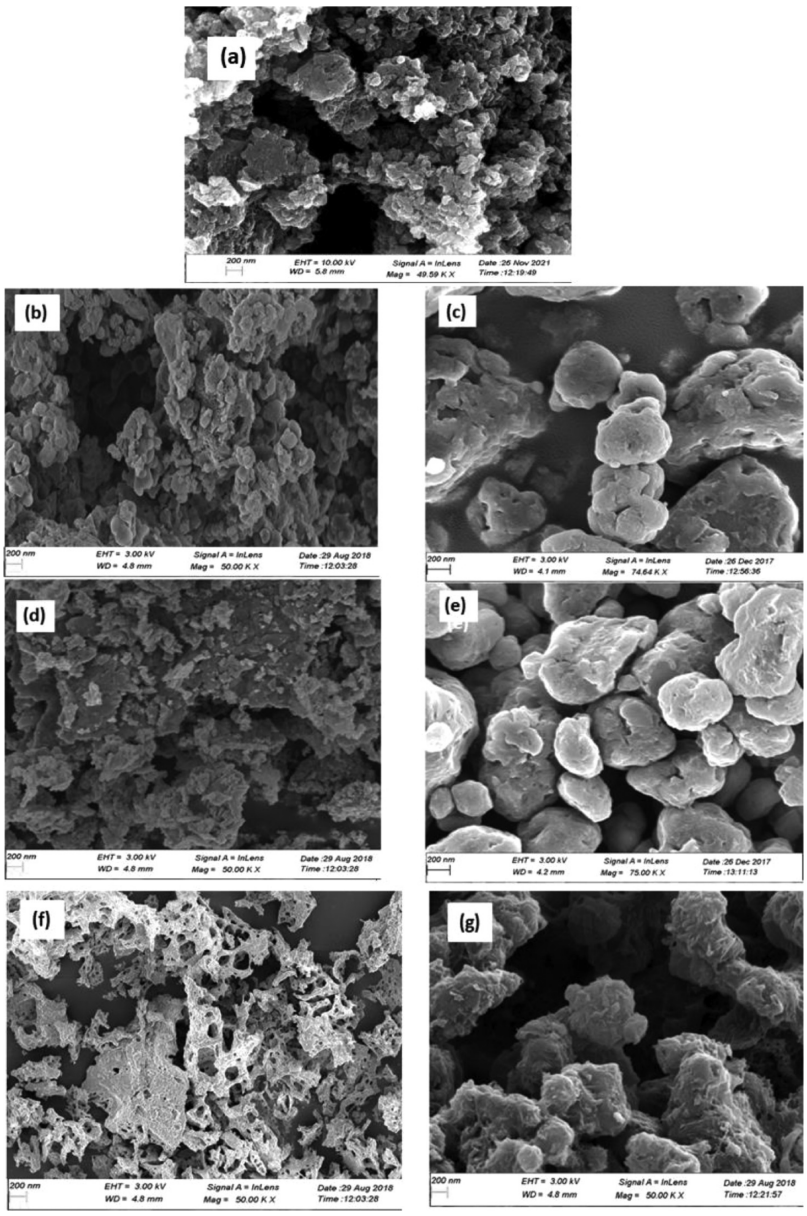

Figure 5. Typical SEM images of (a) PIN, (b) NF, (c) PIN/10NF, (d) NZF, (e) PIN/10NZF, (f) ZF, and (g) PIN/10ZF.

particle in the $Ni_{1-x}Zn_xFe_2O_4$ (x = 0, 0.5, 1) system was taken, and the rings on the diffraction pattern depict a spinel crystal structure of the $Ni_{1-x}Zn_xFe_2O_4$ (x = 0, 0.5, 1) nanoparticles. The appearance of bright diffraction spots in the diffraction circle in the SAED pattern of the NZF system indicates its well-crystalline nature and corresponds to the XRD data. The HRTEM images of the PIN/10 $Ni_{1-x}Zn_xFe_2O_4$ (x = 0, 0.5, 1) nanocomposites (Figure 6g–i) indicate that the in situ emulsion process results in the PIN-layer-wrapped ferrite nanoparticle morphology. The gray layer of PIN gives an impression of an amorphous nature, where no fringes are observed and the black core represents magnetic $Ni_{1-x}Zn_xFe_2O_4$ (x = 0, 0.5, 1) nanoparticles in the nanocomposite due to the different electron penetrabilities.

Magnetic Studies. Detailed magnetic measurements, that is, zero-field cooling (ZFC) and field cooling (FC) magnetization versus temperature and magnetic hysteresis loops (M–H) at room temperatures, have been carried out to study the magnetic properties of the as-synthesized ferrite nanoparticles and their nanocomposites with PIN. Figure 7a–c shows the temperature dependence of magnetization by the ZFC and FC procedures from 5 to 300 K at an applied magnetic field of 500 Oe for the NF, NZF, and ZF nanoparticles. In the ZFC process of NF nanoparticles in Figure 6a, the magnetization of the nanoparticles increases with increasing temperature, and unlike the NZF and ZF nanoparticles, no maximum magnetization is detected in the ZFC process. This indicates that the blocking temperature (T_B) of the NF nanoparticles is above 300 K, which is consistent with the reported data.[63] The blocking temperature (T_B) is a measure of thermal energy required to overcome the magnetic anisotropic barrier of ferro- or ferrimagnetic nanoparticles.[64] This T_B is very sensitive to the grain size distribution and indicates the transition between the superparamagnetic state ($T > T_B$) and the blocked state ($T < T_B$) within the nanoparticle systems. Figure 7a also shows strong irreversibility between FC and ZFC curves, as indicated by the presence of large bifurcation between them, which hints toward the strong exchange interactions associated with the

https://doi.org/10.1021/acsomega.2c00824
ACS Omega 2022, 7, 11473–11490

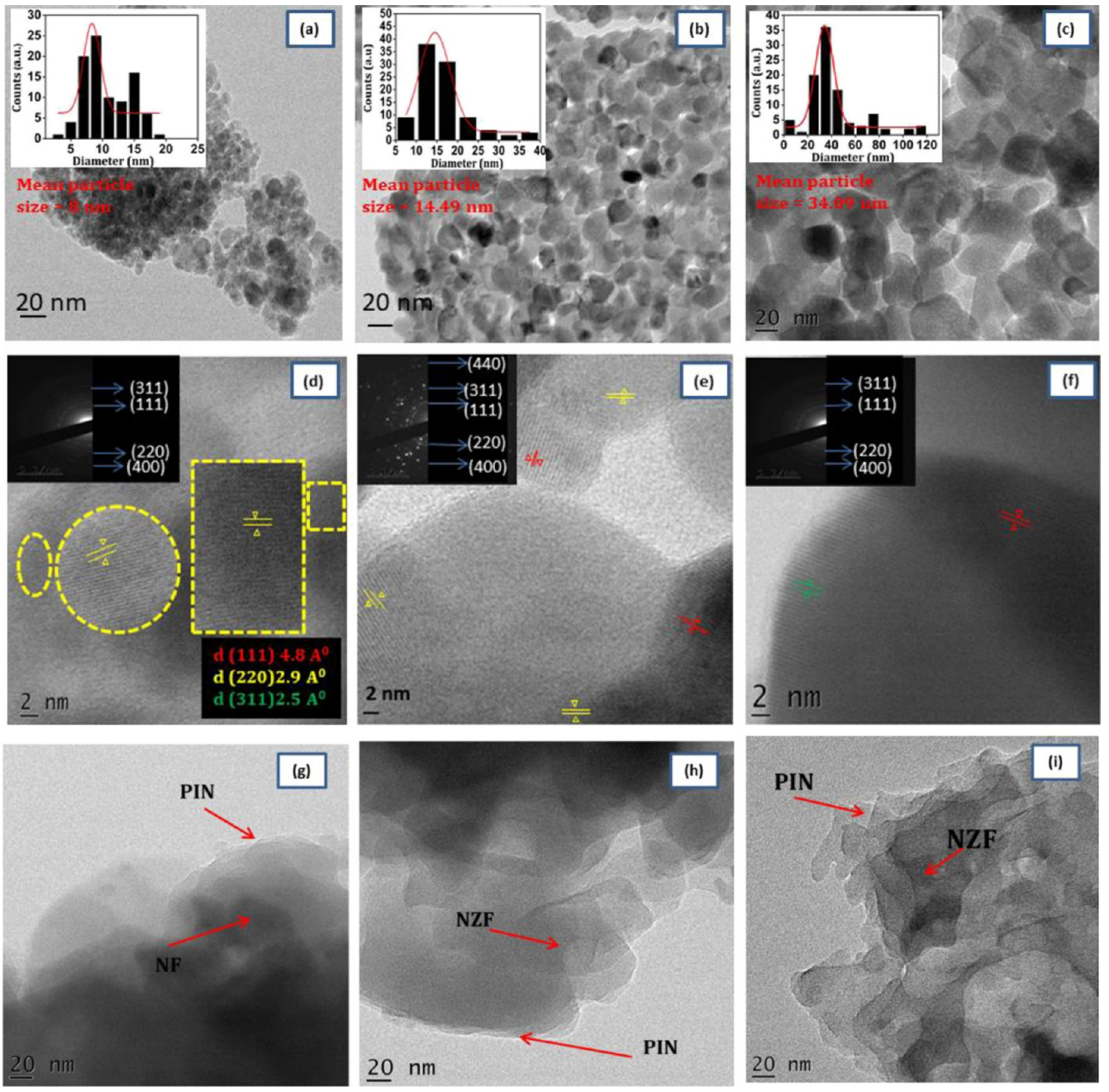

Figure 6. Typical TEM images of (a) NF, (b) NZF, and (c) ZF. The inset in (a–c) shows the particle size distribution. HRTEM images of (d) NF, (e) NZF, and (f) ZF. Inset in (d–f) shows the SAED patterns. TEM images of (g) PIN/10NF, (h) PIN/10NZF, and (i) PIN/10ZF nanocomposites.

particles in the system.[32] Such irreversible behavior originates from the blocking of the magnetization orientation by an anisotropic barrier within the system. The increase in zero field-cooled magnetization (M_{FC}) with decreasing temperature below T_B is also evidence of high magnetocrystalline anisotropy in the NF system, and the large FC magnetization reveals that strong ferrimagnetism occurs in the NF nanoparticles. For the NZF nanoparticles (Figure 7b), M_{ZFC} shows only a small decrease with a broad maximum at T_B = 56.2 K, above which the system shows superparamagnetic behavior. Interestingly, the feature that M_{FC} remains nearly flat below T_B indicates a system with low anisotropy.[36,37] Also, magnetic irreversibility between ZFC and FC curves can be noticed from T_B up to T_{irr} = 245 K, where both curves merge. T_{irr} corresponds to the highest blocking temperature, that is, to that of the largest nanoparticles in the superparamagnetic system with the highest energy barrier.[38] Therefore, the difference between the T_B and T_{irr} values reveals the contribution of the larger particles (broad particle size magnetization as they unblock at higher temperatures and development of ferromagnetic clusters in the NZF nanoparticles). The ZFC curve of ZF nanoparticles (Figure 7c) shows a cusp at the blocking temperature T_B = 16.3 K, as expected for superparamagnetic nanoparticles, below which the system is blocked.[36] However, the large difference between T_B and T_{irr} (at 240 K) is an indication of the existence of ferromagnetic clusters in the ZF nanoparticle system. Furthermore, it is noted that T_B decreases in the order

https://doi.org/10.1021/acsomega.2c00824
ACS Omega 2022, 7, 11473−11490

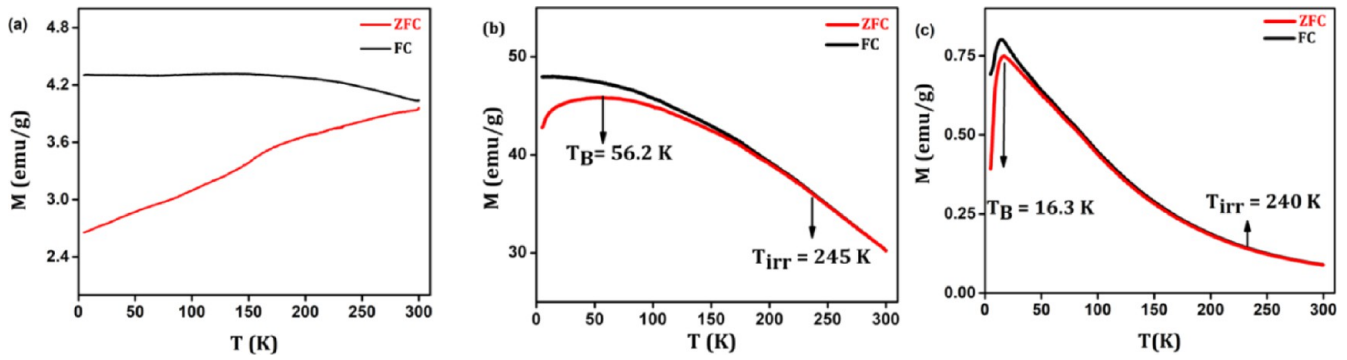

Figure 7. ZFC−FC magnetization of (a) NF, (b) NZF, and (c) ZF at 500 Oe.

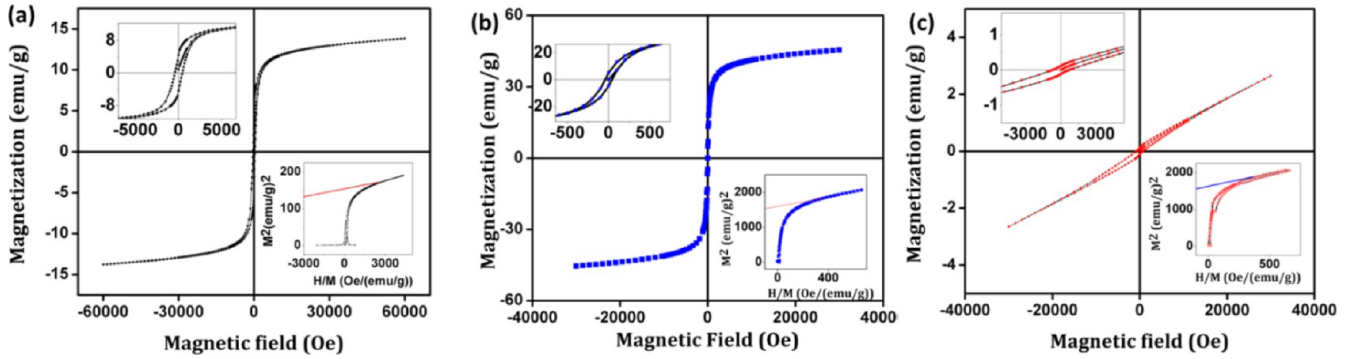

Figure 8. Hysteresis measurements of (a) NF, (b) NZF, and (c) ZF at room temperature. The inset (left) shows an enlarged view of $M-H$ measurements, and the inset (right) illustrates the ABK plot.

Table 2. Blocking Temperature T_B (K), Saturation Magnetization M_s (emu/g), Remanent Magnetization M_r (emu/g), and Coercivity H_c (Oe) for the NF, NZF, and ZF Nanoparticles

nanoparticles	crystallite size (nm)	blocking temperature T_B (K)	sat. magn. M_s (emu/g)	remanent magn. M_r (emu/g)	coercivity H_c (Oe)	squareness ratio (M_r/M_S)
NF	7.5	>300	13.1	6.5	438.5	0.497
NZF	9.6	56.2	45.38	4.85	28.8	0.106
ZF	23.3	16.3		0.106	812.2	

T_BNF > T_BNZF > T_BZF. Interestingly, the ZFC/FC curves of these ferrites reveal that the blocking temperature decreases as the Zn^{2+} concentration increases. A higher T_B value is likely to be indicative of higher magnetocrystalline anisotropy[39] in NF and NZF nanoparticles. When Ni^{2+} ions are substituted by Zn^{2+} ions in the $Ni_{1-x}Zn_xFe_2O_4$ (x = 0, 0.5, 1) system, the magnetic ions of the tetrahedral A site decrease a lot, and the dominant inter-sublattice A−B superexchange interaction becomes weaker.[40] It has been widely reported that the interaction between nanoparticles affects the blocking temperature, and as the strength of interaction weakens, T_B shifts to lower temperatures.[41] To further verify these features, the curves of magnetization versus field were measured at 300 K under an applied field of up to 30 kOe. Figure 8a−c shows the $M-H$ loops for NF, NZF, and ZF nanoparticles at 300 K. Surprisingly, all prepared ferrite nanoparticles displayed magnetic hysteresis at 300 K. The inset (left top) of Figure 8a−c shows an enlarged view of the $M-H$ curve to confirm the presence of a hysteresis loop with coercive field and remanence at room temperature. As expected from the ZFC/FC measurements, the hysteresis loop of the NF nanoparticles is S-shaped, reflecting strong ferrimagnetism, with the coercivity (H_c) and remanent magnetization (M_r) being about 438.5 Oe and 5.6 emu/g, respectively. This $M-H$ curve shows that the magnetization rises sharply as the applied field increases from zero and it weakly increases but does not approach saturation even at a high magnetic field of 60 kOe, indicating high magnetocrystalline anisotropy of the nanoparticles.[42]

The $M-H$ curve of the NZF nanoparticles at 300 K also displays a typical S-shaped loop. In contradiction to the ZFC/FC measurements, the loop exhibits a small coercivity (28.8 Oe) and remanence (4.85 emu/g), indicating weak ferromagnetic behavior at room temperature. For ZF nanoparticles, the magnetization curves have a semilinear representation, which indicates a paramagnetic state with the corresponding large coercivity and small remanent magnetization of 812.2 Oe and 0.106 emu/g, respectively.[65] In addition, the narrow loops indicate the soft magnetic nature of the ZF nanoparticles.[66] The nonsaturating $M-H$ behavior of NZF and ZF nanoparticles even at the applied magnetic fields up to 30 kOe indicate that some of the magnetic nanoparticles of these ferrite samples are in the superparamagnetic state. However, the existence of the coercive field in these systems implies that the rest of the particles are blocked due to the overcoming of the thermal energy by their anisotropy energy even at room temperature.[43] This discrepancy between the hysteresis at 300 K and the blocking temperature for NZF and ZF nanoparticles is due to the broad size distribution and consequently, these

https://doi.org/10.1021/acsomega.2c00824
ACS Omega 2022, 7, 11473−11490

samples show different blocking temperatures. For a better understanding of the magnetic behavior of the prepared ferrite samples at room temperature, the Arrott–Belov–Kouvel (ABK) plot (M^2 vs H/M) was made and is shown in the lower inset of Figure 8a–c. The ABK plot of all samples shows a strong convex curvature with a finite spontaneous magnetization, which is a signature of a ferromagnetic phase of these samples.[63] The magnetic properties measured for NF, NZF, and ZF nanoparticles are listed in Table 2, and a comparison of the M–H plots is shown in Figure 9. Interestingly, it can be

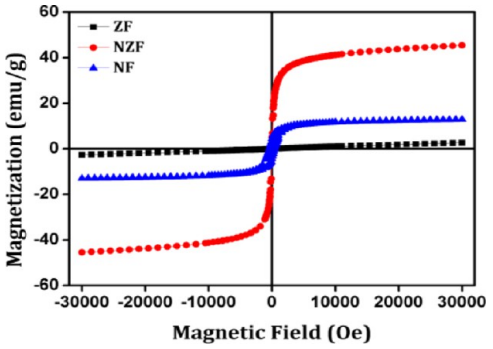

Figure 9. Comparison of hysteresis measurements of NF, NZF, and ZF at room temperature.

seen in Figure 9 that the magnetization of NZF is very high as compared to NF and ZF nanoparticle systems. It is known that in ferrites, the magnetic moment comes mainly from the parallel uncompensated electron spin of individual ions.[67] As nonmagnetic Zn^{2+} ions are introduced into the $Ni_{1-x}Zn_xFe_2O_4$ (x = 0, 0.5, 1) system, they push more Fe^{3+} ions from tetrahedral A sites to octahedral B sites, and thereby, the magnetic moment of the B site increases. Hence, the total magnetization ($M_{oh} - M_{tet}$) of the $Ni_{1-x}Zn_xFe_2O_4$ (x = 0, 0.5, 1) system increases due to the increase of inter-sublattice A–B superexchange interaction between the magnetic ions of A and B sublattices. This increase in saturation magnetization is in good agreement with Neel's collinear two-sublattice model.[62]

Furthermore, with an increase in the Zn concentration from x = 0.5 to x = 1, the magnetization gradually decreases from 45.38 to 2.6 emu/g. In the ZF system, more Zn^{2+} cations occupy in the tetrahedral site, and thereby, the magnetic ions of the A-site decrease a lot, the dominant inter-sublattice A–B superexchange interaction diminishes, and accordingly, the intra-sublattice B–B superexchange interaction strengthens. This, in turn, results in the development of random spin canting on the B site toward the direction of spins of the A-site, and therefore, the magnetization decreases. It is also observed that the behavior of the coercivity was not linear. It decreases as the concentration of Zn^{2+} changes from x = 0 to x = 0.5, and then, at x = 1, the value of the coercivity was maximum. The coercivity of the ZF system is almost 2 orders of magnitude higher than that of the NF system. The magnetic domain walls and their magnetic moments significantly contribute to the variations in the coercivity and magnetocrystalline anisotropy in nanoferrites. The squareness ratio (M_r/M_S) is also calculated, and its values are shown in Table 2. It has been reported that a squareness ratio near or above 0.5 indicates that the material is around the single magnetic domain size and that below 0.5 can be attributed to the formation of a multidomain structure.[68] The squareness ratios for NF and NZF are 0.497 and 0.106, respectively, indicating that the NF nanoparticles have a single domain structure, whereas the NZF nanoparticles possess a multidomain structure, in which the domain wall movement allows for an easier change in orientation with the applied field. To understand the correlation of magnetization with particle loading, $M(H)$ hysteresis loops of the PIN/$Ni_{1-x}Zn_xFe_2O_4$ (x = 0, 0.5, 1) nanocomposites were recorded under an applied magnetic field up to 30 kOe at room temperature and compared with the respective nanoparticles, as presented in Figure 9. According to Figure 10a–c, the magnetic nanocomposites present a hysteresis loop similar to the ferrite nanoparticles. This reveals the fact that the magnetic properties of the nanoparticles were preserved in the nanocomposites since the polymeric matrix of PIN is originally a diamagnetic material. The influence of the nanoparticle loading in the polymer matrix on the saturation magnetization (M_s), remnant magnetization (M_r), coercivity (H_c), and squareness ratio (M_r/M_S) is tabulated in Table 3. It is worth noting that the saturation magnetization of nanocomposites is lower than that of pure ferrite nanoparticles and depends mainly on the fraction of the magnetic nanoparticles in the matrix. As the PIN matrix is nonmagnetic, it plays a part in isolating the magnetic fillers, leading to the transformation of the collinear ferromagnetic order of the magnetic nanoparticles into a noncollinear arrangement with a disruption of the ferromagnetic order.[69] Therefore, the demagnetization effect of the matrix is notable. Interestingly, the magnetization of the PIN/NZF nanocomposites is much higher compared to the PIN/NF and PIN/ZF nanocomposites with the same filler

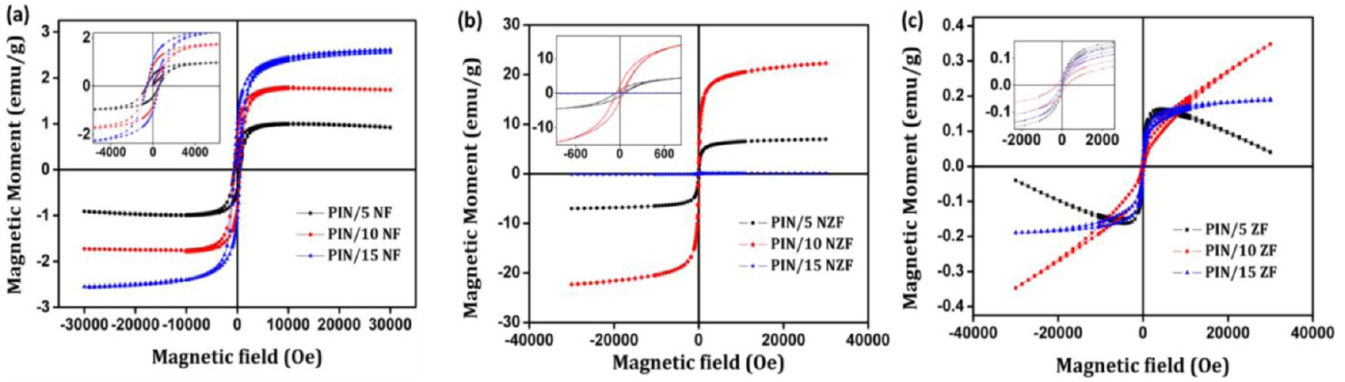

Figure 10. Hysteresis measurements of (a) PIN/NF, (b) PIN/NZF, and (c) PIN/ZF composites with 5, 10, and 15 wt % ferrite ratios at room temperature. The inset shows an enlarged view of the M–H measurement.

https://doi.org/10.1021/acsomega.2c00824
ACS Omega 2022, 7, 11473–11490

Table 3. Saturation Magnetization M_s (emu/g), Remanent Magnetization M_r (emu/g), and Coercivity H_c (Oe) of the PIN/NF, PIN/NZF, and PIN/ZF Nanocomposites

samples	crystallite size (nm)	sat. magn, M_s (emu/g)	remanence, M_r (emu/g)	coercivity H_c (Oe)	squareness ratio (M_r/M_S)
PIN/5NF	38.4	0.69	0.43	557	0.623
PIN/10NF	34.5	2.6	1.14	593	0.48
PIN/15NF	30.9	1.73	1.0	584	0.578
PIN/5NZF	30.7	7.05	0.86	61.85	0.121
PIN/10NZF	23.1	22.5	2.3	45.47	0.102
PIN/15NZF	21.0	0.41	0.018	99	0.043
PIN/5ZF	26.2		0.007	26	
PIN/10ZF	26.1		0.02	232	
PIN/15ZF	26.0	0.19	0.022	96	0.115

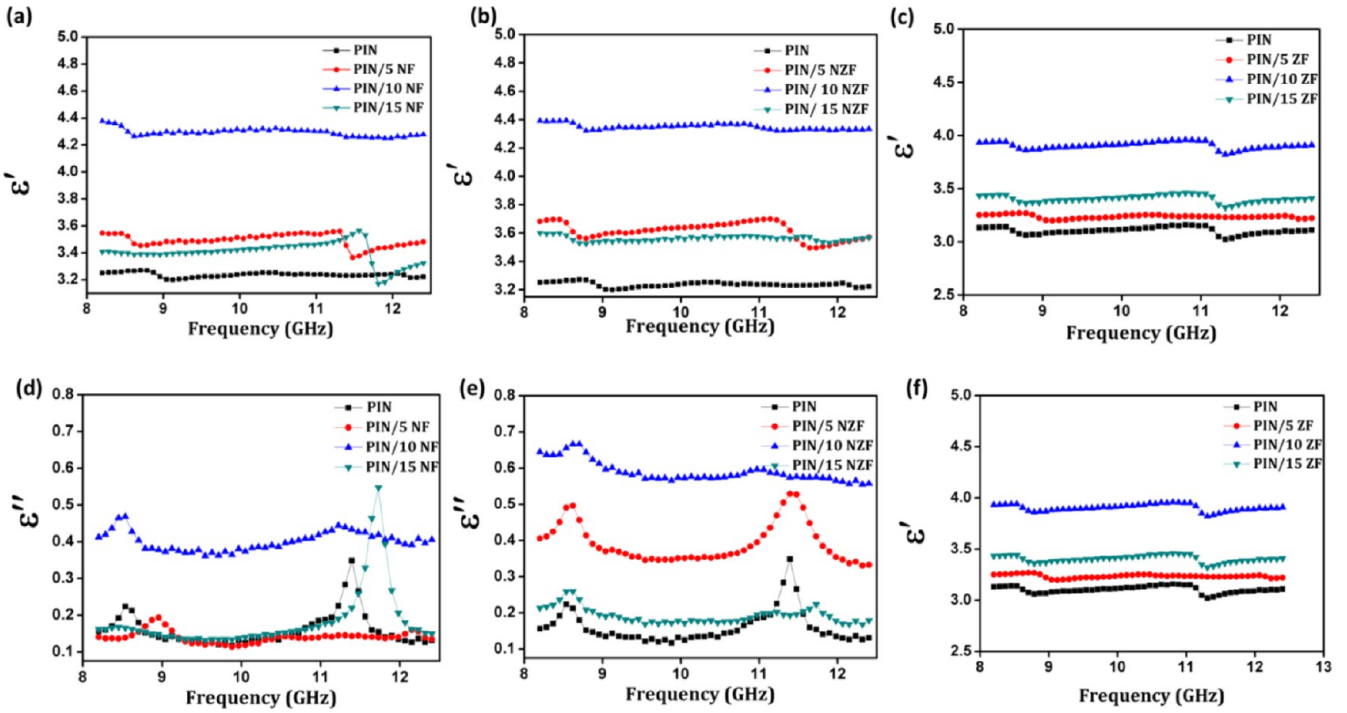

Figure 11. Behavior of the real part of complex permittivity (a–c) and imaginary part of complex permittivity (d–f) of PIN and PIN/$Ni_{1-x}Zn_xFe_2O_4$ (x = 0, 0.5, 1) nanocomposites with 5, 10, and 15 filler ratios as a function of frequency.

wt % over the entire magnetic field range. Additionally, as the content of ferrite nanoparticles in the polymer matrix increases, the particle's tendency toward agglomeration increases. The formation of small clusters of nanoparticles reduces the interfacial area, and therefore, the interfacial interaction is weakened.[70] This explains why the M_s enhancement is the strongest in the 10 wt % nanocomposites, in which the nanoparticles are more completely dispersed, compared to 5 and 15 wt % nanocomposites. On the other hand, the coercivity (H_c) of the nanocomposites exhibits a different behavior from saturation magnetization. For the PIN/NZF nanocomposites, the coercivity increases with the filler content and is slightly higher than that of the pure NZF due to the magnetic strain of the PIN polymer chain.[71] In the nanocomposites, the diamagnetic phase of PIN acts as a barrier for domain interactions and domain misalignment, similar to the presence of nonmagnetic oxide additives in ferrites, which results in a higher coercivity.[72] It is known that the interface structure, constitution, particle size and shape, magnetic anisotropy, and magnetostriction are the main factors that affect coercivity.[70] Here, this typical behavior can be mainly attributed to the interface structure and magnetostrictive coupling. The magnetostrictive effect causes distortion of the crystal lattices of NZF under an applied magnetic field, which in turn leads to local strains or stresses between the PIN matrix and NZF magnetic phases via intimate mechanical contact. As a result, higher filler loading leads to higher coercivity. Surprisingly, for nanocomposites of PIN/ZF, it is observed that the coercivity is hardly lower compared to pure ZF and increases up to 10 wt % filler addition and then decreases. This trend is due to the interparticle dipolar interaction within the PIN/ZF nanocomposites with good dispersion of single-domain ZF nanoparticles, consistent with the particle loading-dependent coercivity in the nanocomposites. Compared with the 10 wt % nanocomposite, the lower coercivity in the 15 wt % nanocomposite arises from the demagnetizing role played by the dipolar interaction, as simulated by Kechrakos and Trohidou.[73,74] These interactions result in the formation of ferromagnetic clusters of particles with low anisotropy, as explained earlier, which aids in the magnetization reversal, and the coercivity reduces relative to the noninteracting case. Similarly, dipolar and exchange forces

https://doi.org/10.1021/acsomega.2c00824
ACS Omega 2022, 7, 11473–11490

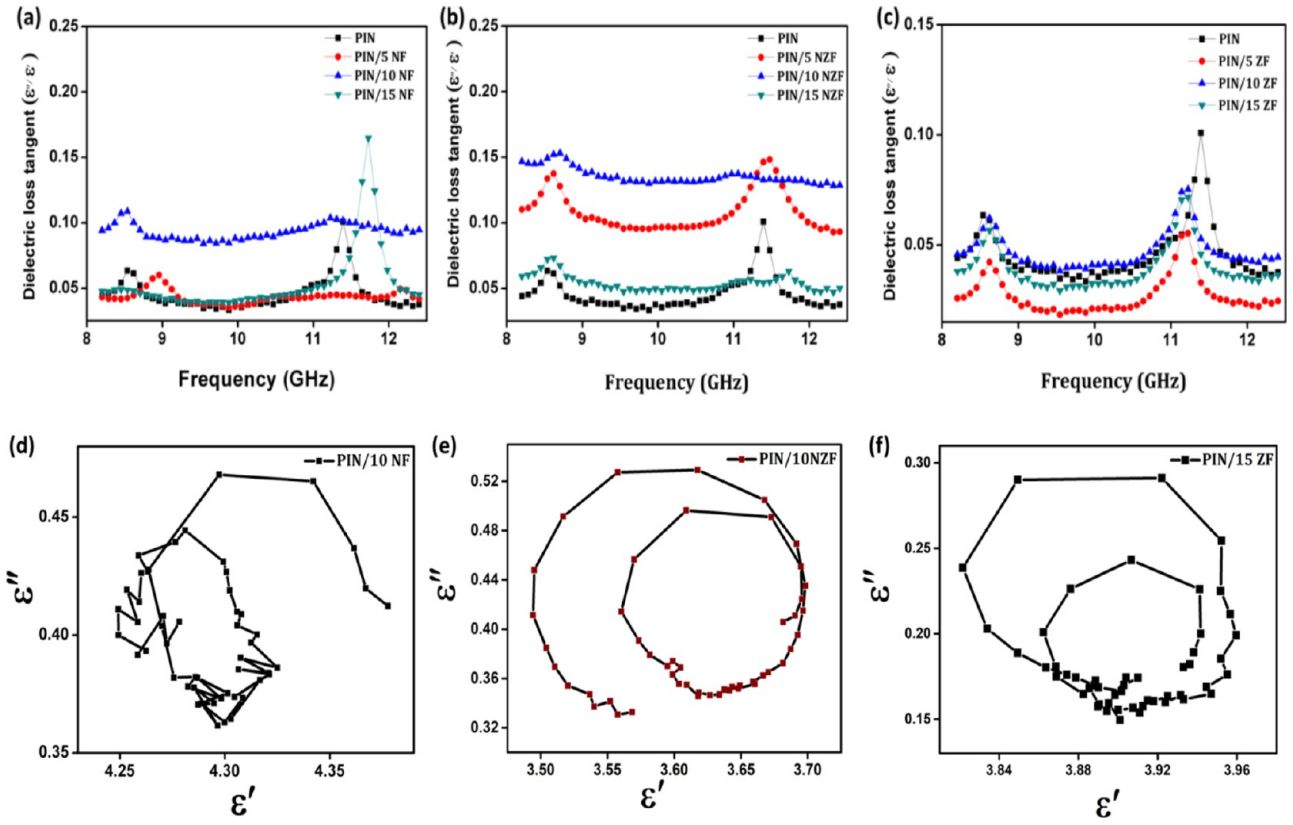

Figure 12. Dielectric loss tangent (a–c) of PIN and PIN/$Ni_{1-x}Zn_xFe_2O_4$ (x = 0, 0.5, 1) nanocomposites with 5, 10, and 15 filler ratios. Cole–Cole plot of (d) PIN/5NF, (e) PIN/10NZF, and (f) PIN/15ZF.

also compete in producing a similar trend for the concentration dependence of the remanence in nanocomposites. In the present study, the squareness ratio for PIN/5NF, PIN/10NF, and PIN/15NF, which also have the highest H_c values, is found to be near and above 0.5, indicating that these samples have a virtually single-domain structure, while all the other compositions (lower H_c) possess ratios less than 0.5, suggesting that these have a multidomain structure.

MA Properties. In general, the impedance matching and attenuation characteristics of high-performance microwave absorbers are determined by the relative complex permittivity ($\varepsilon_r = \varepsilon' - j\varepsilon''$) and relative complex permeability ($\mu_r = \mu' - j\mu''$) and the complementarities between them. The real part (ε' or μ') is mainly dependent on the amount of electrical or magnetic energy stored in the material, and the imaginary part (ε'' or μ'') is connected to the dissipation of electrical and magnetic energy.[75,76] Complex permittivity studies of PIN and PIN/$Ni_{1-x}Zn_xFe_2O_4$ (x = 0, 0.5, 1) nanocomposites are shown in Figure 11a–f. In Figure 10, it is evidenced that PIN nanocomposites show better dielectric performance as compared to pristine PIN. Such enhanced dielectric permittivity mainly arises from strong dipole orientation and space charge polarization (interfacial polarization) developed in the system.[77] Dipoles, namely, the bound charges present in conjugated polymers, cannot reorient themselves quickly to respond to the applied electric field, resulting in dipole orientation polarization.[78] The incorporation of insulating ferrites into the conducting PIN matrix may result in the formation of more interfaces and a heterogeneous system due to some space charges accumulating at the interface. It is worth noting that the ε' and ε'' values of PIN/10 $Ni_{1-x}Zn_xFe_2O_4$ (x = 0, 0.5, 1) composites are higher than 5 and 15 wt % filler content. The higher values of ε' and ε'' arise due to the difference in the relative dielectric constant of ferrite and PIN. This leads to the accumulation of more space charge and thereby strong orientational polarization in composites. Consequently, the MA of the composite will be enhanced. It is clear that the ε'' values of all composites show an initial gradual increase up to 8.5 GHz and then decrease sharply between 8.5 and 9 GHz. Furthermore, the composites introduce a broad band between 9 and 11 GHz, then decrease, and finally show a marginal increase from 11.5 GHz onward. The reason for such fluctuations can be explained as the fall off in the ability of the dipoles to maintain the in-phase movement with the electric vector of the incident EM wave, which pulsates rapidly.[79] The dielectric tangent loss (tan δ_e) of PIN and PIN/$Ni_{1-x}Zn_xFe_2O_4$ (x = 0, 0.5, 1) composites nanocomposites were calculated based on the data shown in Figure 11a–f, and the results are shown in Figure 12a–c. As demonstrated in Figure 12, the tan δ_e values of the PIN/10NZF nanocomposite are higher than those of all other samples. Another interesting phenomenon is that the tan δ_e value of composites shows weak fluctuations at a low frequency (8–9 GHz)and a strong peak at a high frequency (11–12 GHz), and each semicircle is related to a Debye dipolar relaxation.[76,80] Figure 12d–f shows the curve characteristics of ε' versus ε'' (Cole–Cole plot) for the PIN/5NF, PIN/10NZF, and PIN/15ZF samples. It can be seen that the PIN/10NZF composite with well-dispersed nanoparticles displays ternary dielectric relaxation processes and contributes to the enhancement of MA in the composite.[81] Ferrite nanoparticles in the PIN matrix have an enormous number of interfaces and

https://doi.org/10.1021/acsomega.2c00824
ACS Omega 2022, 7, 11473–11490

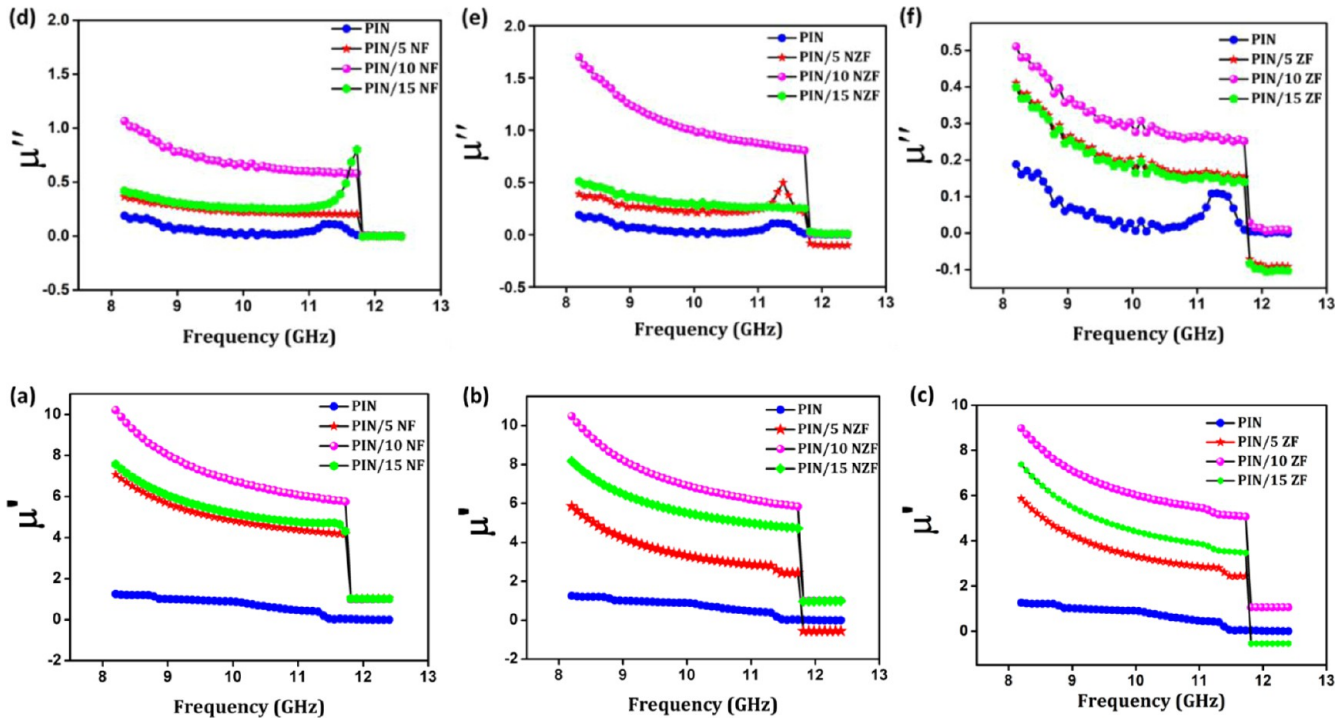

Figure 13. Behavior of the real part of complex permeability (a–c) and imaginary part of complex permeability (d–f) of PIN and PIN/$Ni_{1-x}Zn_xFe_2O_4$ (x = 0, 0.5, 1) nanocomposites with 5, 10, and 15 filler ratios as a function of frequency.

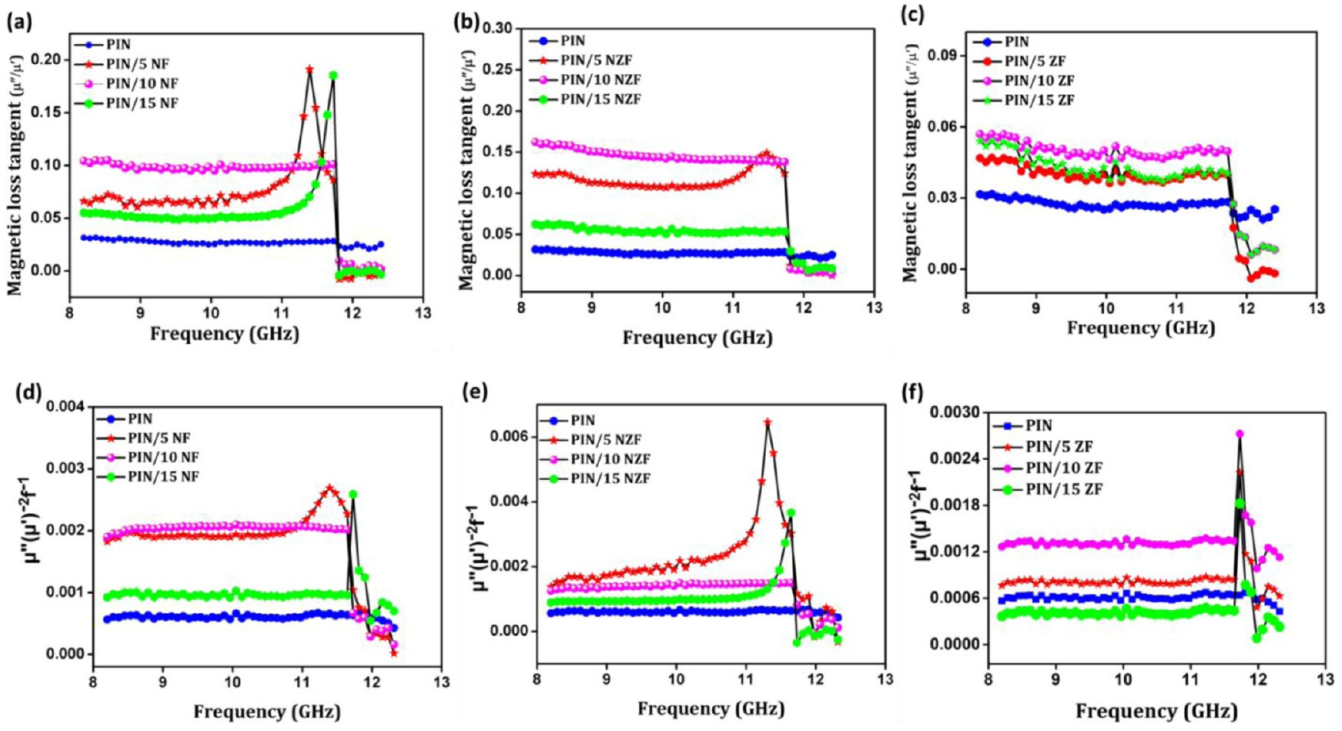

Figure 14. Magnetic tangent loss (a–c) of PIN and PIN/$Ni_{1-x}Zn_xFe_2O_4$ (x = 0, 0.5, 1) nanocomposites with 5, 10, and 15 filler ratios. The value C_0 of (d) PIN/NF, (e) PIN/NZF, and (f) PIN/ZF nanocomposites as a function of frequency.

defects, such as vacancies and microporosities, which can cause a change of positive and negative space charge distribution at the interfaces.[82] Under a sufficient electromagnetic field, the electrons that reside on the nitrogen atoms of the may gain enough energy to surmount the interfaces, thus resulting in the formation of an additional relaxation process. Figure 12d,f shows that the Cole–Cole semicircles are distorted, suggesting that besides the dielectric relaxation, other mechanisms such as conductance loss and the interfacial polarization, may contribute to the permittivity spectra too.[83] That is to say, dielectric relaxation processes and interfacial polarization are expected to result in the enhancement of dielectric loss.[84]

Figure 13a–f shows the variation in the real (μ') and imaginary (μ'') parts of permeability with frequency for PIN

https://doi.org/10.1021/acsomega.2c00824
ACS Omega 2022, 7, 11473–11490

and PIN/$Ni_{1-x}Zn_xFe_2O_4$ (x = 0, 0.5, 1) nanocomposites at 5, 10, and 15 wt % filler ratios. It can be observed that the μ' and μ'' values of PIN nearly remain constant over the whole frequency range. However, the μ' and μ'' values of all PIN/$Ni_{1-x}Zn_xFe_2O_4$ (x = 0, 0.5, 1) nanocomposites exhibit a gradual decrease with the increase of frequency at the low-frequency region and further change into a rapid descending slope at the high-frequency region. It is also observed that the μ'' values for the PIN/15NF and PIN/5NZF composites show peaks at higher-frequency regions. The maximum value of μ'' is 0.98 at 11.8 GHz for PIN/15NF and 0.5 at 11.5 GHz for PIN/5NZF, respectively. The μ' and μ'' values of each nanocomposite are higher than those of nonmagnetic PIN over the whole frequency range. It is noted that the μ' and μ'' values of the PIN/10NZF composite are higher than those of all other samples, which confirm the existence of greater magnetic losses in the nanocomposite. It is well known that magnetic parameters such as saturation magnetization (M_s) and coercivity (H_c) cannot be directly linked with magnetic loss, whereas initial permeability (μ_i), is usually linked to predict the magnetic loss ability[78] and can be expressed by

$$\mu_i = \frac{M_s^2}{(aKH_cM_s) + b\lambda\tau} \quad (2)$$

where a and b are two constants determined by the material composition, λ is the magnetostriction constant, and τ is an elastic strain parameter of the crystal. From eq 2, it can be concluded that initial permeability can be enhanced either by increasing saturation magnetization or by reducing coercivity. It is evident from Table 2 that the PIN/10NZF composites have high M_s and low H_c values and result in higher magnetic loss values. As shown in Figure 13a–f, the μ' and μ'' values of PIN/5NZF and PIN/15ZF nanocomposites are negative at the high-frequency region, indicating the eddy current effect and strong magnetic resonance loss in the microwave region for these composites. The negative μ'' values arise from induced magnetic energy going out of the absorber; meanwhile, the incident electromagnetic energy is consumed in the absorber due to the eddy current loss. The magnetic loss tangent (tan δ_m) of PIN and PIN/$Ni_{1-x}Zn_xFe_2O_4$ (x = 0, 0.5, 1) was calculated based on the data (Figure 13a–f), and the results are shown in Figure 14a–c. It can be seen that tan $\delta_m = \mu''/\mu'$ of all composites gives a constant value at a low-frequency region and then exhibits a large drop at 11.7 GHz, which corresponds to the rapid descending slope in μ' and μ'' curves. Generally, hysteresis loss, domain wall resonance, natural ferromagnetic resonance, and eddy current effect are the main reasons for the magnetic loss in micro-/nanostructured materials.[79] In our system, the contributions from eddy current effect and natural resonance are taken into consideration because the hysteresis loss comes from irreversible magnetization and is imperceptible in the weak EM field, whereas domain wall resonance is only found to occur in multidomain materials at a much lower frequency (1–100 MHz).[79,85] The eddy current loss of a magnetic particle with diameter D, less than the skin depth, is revealed by the equation

$$\frac{\mu'}{\mu''} \propto \frac{\mu' f D^2}{\rho} \quad (3)$$

where f is the applied frequency and ρ is the electric resistivity of the particle. It is well known that if the magnetic loss results from the eddy current effect, the variation of C_0 ($C_0 = \mu''(\mu')^{-2}f^{-1}$) with frequency should be constant. As shown in Figure 14d–f, the values of C_0 remain approximately constant in the frequency range of 8.0–11 GHz. However, when f > 11 GHz, the curves show slight fluctuations. Thus, it can be concluded that the magnetic loss at the low-frequency range is caused by the eddy current effect, and the peaks at the high-frequency range are ascribed to the natural resonance. It is also noted that PIN/5NZF and PIN/15ZF show much stronger fluctuation in the high-frequency region.

The MA property of an absorber material is measured by the parameter reflection loss (RL), which is obtained from the following equations based on transmission line theory[28]

$$Z_{in} = Z_0\sqrt{\frac{\mu_r}{\varepsilon_r}}\tanh\left[f\left(\frac{2\pi fd}{c}\right)\sqrt{\mu_r\varepsilon_r}\right] \quad (4)$$

$$\mathrm{RL\ (dB)} = 20\log\left|\frac{Z_{in} - Z_0}{Z_{in} + Z_0}\right| \quad (5)$$

where Z_{in} is the normalized input impedance of the absorber, Z_0 is the impedance of free space, μ_r and ε_r are the relative complex permeability and permittivity of the absorber, respectively, c is the velocity of light, and d is the thickness of the absorber. It is noticed that when the RL of the absorber is lower than −10 dB, more than 90% of the electromagnetic energy is absorbed, and this area can be seen as an effective EA bandwidth. Figure 15 shows the calculated theoretical RL of

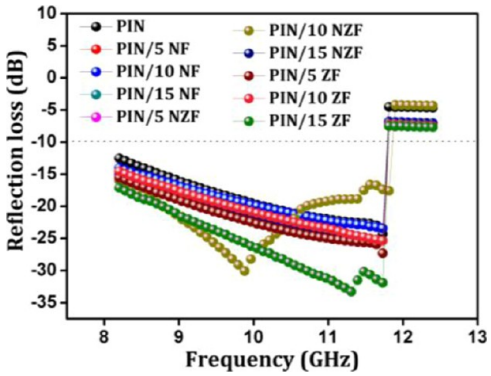

Figure 15. MA properties of PIN and PIN/$Ni_{1-x}Zn_xFe_2O_4$ (x = 0, 0.5, 1) nanocomposites with 5, 10, and 15 filler ratios.

the PIN and PIN/$Ni_{1-x}Zn_xFe_2O_4$ (x = 0, 0.5, 1) nanocomposites with filling amounts of 5, 10, and 15 wt % in the 8–12 GHz frequency range (X band). The results demonstrate that the as-synthesized PIN/10NZF and PIN/15ZF nanocomposites show a better MA performance than those of the pristine PIN and other composites. The PIN/10NZF and PIN/15ZF composites exhibit a maximum absorption of −30.52 dB at 9.86 GHz and −33.08 dB at 11.3 GHz, respectively. This may be attributed to the heterogeneous interfaces between the PIN and nanoparticles, as well as the good dispersion of ferrite nanoparticles in the PIN matrix. Furthermore, the better performance of a microwave absorber is mainly due to the good matching between dielectric loss and magnetic loss and thereby matching of impedance upon the irradiation on the surface of the material.

Microwave Shielding Performance. The SE of PIN and PIN/$Ni_{1-x}Zn_xFe_2O_4$ (x = 0, 0.5, 1) with the filling amounts of 5, 10, and 15 wt % in the 8–12 GHz frequency range (X band)

https://doi.org/10.1021/acsomega.2c00824
ACS Omega 2022, 7, 11473–11490

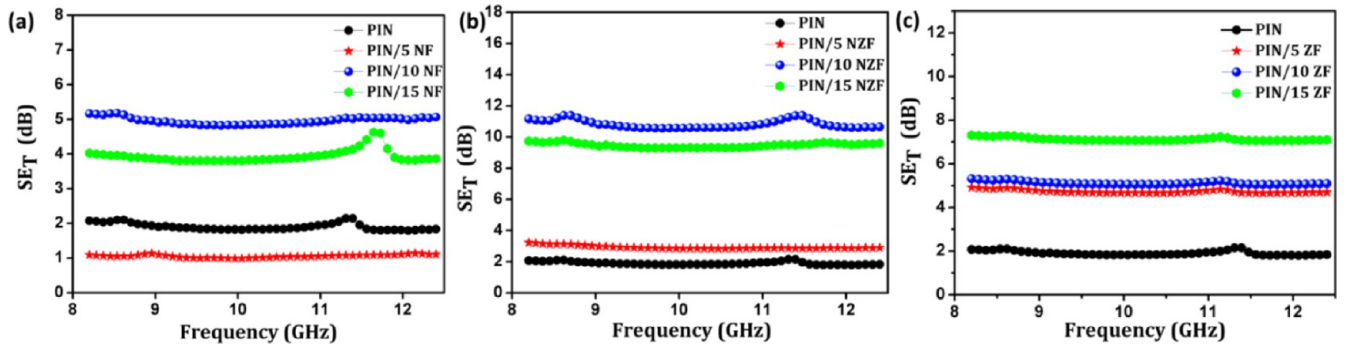

Figure 16. Microwave shielding (SE_T) behavior of (a) PIN/NF, (b) PIN/NZF, and (c) PIN/ZF nanocomposites with 5, 10, and 15 w % ferrite ratios.

is presented in Figure 16. The SE is measured as the ability of a material to attenuate the intensity of EM waves,[77] and the total SE (SE_T) is the summation of shielding by absorption (SE_A), reflection (SE_R), and multiple reflections (SE_{MR}) and is expressed as[75,86]

$$SE_T = SE_A + SE_R + SE_{MR} \quad (6)$$

The SE_T, SE_R, and SE_A can be estimated using scattering parameters (S_{11} or S_{22} and S_{12} or S_{21}) obtained by vector network analyzer (VNA) and are expressed as

$$SE_T\ (dB) = 10 \log \frac{1}{S_{12}^2} = 10\ \log \frac{1}{S_{21}^2} \quad (7)$$

$$SE_R\ (dB) = 10 \log \frac{1}{1 - S_{11}^2} \quad (8)$$

$$SE_A\ (dB) = 10 \log \frac{1 - S_{11}^2}{S_{12}^2} \quad (9)$$

The SE_T of pristine PIN is only 2.07 dB, presenting poor shielding property. As compared to the lower SE_T of PIN, the SE_T of the composite increases, with the filler content exhibiting excellent frequency stability in the measured frequency range. Pure PIN is nonmagnetic, and its contribution to MA is mostly because of dielectric loss. Therefore, the composite using PIN and ferrite exhibits both enhanced dielectric losses and magnetic losses in a wide frequency range because of enhanced interfacial polarization between the ferrite nanoparticles and PIN. By comparing these curves, it is found that upon increasing the addition of ferrite nanoparticles to PIN from 5 to 10 wt %, the SE value was significantly enhanced. For the PIN/NF composites, the SE improves from 1.08 to 5.1 dB, whereas for the PIN/NZF composites, the respective enhancement is from 3.2 to 11.1 dB. Upon further increase of the filler amount to 15 wt %, the SE_T of PIN/NF and PIN/NZF nanocomposites reduced to 4.1 and 9.2 dB, respectively. However, the SE_T value of PIN/15ZF improved to 7.59 dB. Surprisingly, the PIN/10NZF composite showed a much improved SE of 11.6 dB in comparison to other composites. When the material used as the EMI shield tends to be conductive, it does not imply that conductivity is the critical criterion for EMI shielding as conduction requires connectivity between the fillers.[77] The dependence of SE on the conductivity can be expressed as[13,77]

$$SE_A\ (dB) = 20\frac{d}{\delta} \log e = 20d\sqrt{\frac{\mu_r \omega \sigma_{AC}}{2}} \log e \quad (10)$$

$$SE_R\ (dB) = 10\ \log\left(\frac{\sigma_{AC}}{16\mu_r \omega \varepsilon_0}\right) \quad (11)$$

where d is the thickness of the shield, μ_r is the magnetic permeability, δ is the skin depth, $\sigma_{AC} = \omega\varepsilon_0\varepsilon''$ is the frequency-dependent conductivity, ε'' is the imaginary part of permittivity (dielectric loss factor), ω is the angular frequency ($\omega = 2\pi f$), and ε_0 is the permittivity of the free space. The magnitude of SE_A is dependent on the product of the electrical conductivity, dielectric permittivity, and permeability of the shield material. The sample with 10 wt % of ferrite in PIN shows an evident electrical conductivity enhancement, combined with the SE results. At this loading, nanoparticles within the matrix closely interact due to the excellent dispersion of nanoparticles and thereby form more effective conductive networks. This implies that electrical percolation is one of the necessary conditions for shielding.[87] Hence, we can construct multilayered composites that will definitely show better shielding due to increased attenuation of EM waves through impedance mismatch at the interface of two composites. A greater impedance mismatch increases the reflectance of EM waves into the composite, resulting in improved attenuation of the EM wave before it propagates through the multilayered stack.[88] In general, the intrinsic electrical conductivity of the conjugated polymers in the MA band (100 MHz to 20 GHz) can make them very promising materials. Therefore, it can be suggested that a combination of a conducting PIN matrix with $Ni_{1-x}Zn_xFe_2O_4$ (x = 0, 0.5, 1) ferrite nanoparticles can balance impedance matching conditions and offer microwave shielding at the other frequency range beyond 8−12 GHz.

CONCLUSIONS

Nanocomposites consisting of $Ni_{1-x}Zn_xFe_2O_4$ nanoparticles incorporated in PIN were successfully synthesized by the in situ emulsion polymerization method. The as-prepared nanocomposites were characterized through Fourier transform infrared spectroscopy (FTIR), UV−vis spectroscopy, XRD, SEM, HRTEM, and VSM. The as-prepared nanocomposites exhibit efficient MA properties with a minimum RL of up to −33 dB. The PIN/10 NZF nanocomposite demonstrates strong microwave shielding properties in 8−12 GHz with a SET value of 11.5 dB, and this high shielding property mainly results from the high dielectric and magnetic losses in the composites. The magnetic and MA properties depend on the concentration of the $Ni_{1-x}Zn_xFe_2O_4$ nanoparticles in the polymer composite. These nanocomposites can offer an

https://doi.org/10.1021/acsomega.2c00824
ACS Omega 2022, 7, 11473−11490

effective way to design high-performance functional materials to facilitate the research in electromagnetic shielding and MA.

AUTHOR INFORMATION

Corresponding Author

Pradeepan Periyat − *Department of Environmental Studies, Kannur University, Kannur, Kerala 670567, India;* orcid.org/0000-0001-8546-0994; Email: pperiyat@uoc.ac.in, pperiyat@kannuruniv.ac.in

Authors

Anjitha Thadathil − *Department of Chemistry, University of Calicut, Thenhipalam, Kerala 673635, India*

Jithesh Kavil − *Department of Chemistry, University of Calicut, Thenhipalam, Kerala 673635, India*

Govind Raj Kovummal − *Department of Chemistry, Malabar Christian College, Calicut, Kerala 673001, India;* orcid.org/0000-0002-2978-2822

Chamundi P. Jijil − *Department of Chemistry, University of Calicut, Thenhipalam, Kerala 673635, India*

Complete contact information is available at: https://pubs.acs.org/10.1021/acsomega.2c00824

Notes

The authors declare no competing financial interest.

ACKNOWLEDGMENTS

A.T. is grateful to the CSIR for the CSIR-JRF. The authors are thankful to K. P. Surendran and Aparna P. N. for MA measurements and Safna Hussain K. P. for her suggestion during the manuscript preparation. The authors are also thankful to the Central Sophisticated Instrumentation Facility, University of Calicut, for various measurements.

REFERENCES

(1) Soares, B. G.; Barra, G. M. O.; Indrusiak, T. Conducting polymeric composites based on intrinsically conducting polymers as electromagnetic interference shielding/microwave absorbing materials—A review. *J. Compos. Sci.* **2021**, *5*, 173.

(2) Sushmita, K.; Madras, G.; Bose, S. Polymer nanocomposites containing semiconductors as advanced materials for EMI shielding. *ACS Omega* **2020**, *5*, 4705−4718.

(3) Shi, J.; Li, Z.; Sang, D. K.; Xiang, Y.; Li, J.; Zhang, S.; Zhang, H. THz photonics in two dimensional materials and metamaterials: properties, devices and prospects. *J. Mater. Chem. C* **2018**, *6*, 1291−1306.

(4) Xiang, Y.; Dai, X.; Guo, J.; Zhang, H.; Wen, S.; Tang, D. Critical coupling with graphene-based hyperbolic metamaterials. *Nat. Mater.* **2014**, *4*, 5483.

(5) Peymanfar, R.; Karimi, J.; Fallahi, R. Novel, promising, and broadband microwave-absorbing nanocomposite based on the graphite-like carbon nitride/CuS. *J. Appl. Polym. Sci.* **2020**, *137*, 48430.

(6) He, P.; Cao, M.-S.; Cai, Y.-Z.; Shu, J.-C.; Cao, W.-Q.; Yuan, J. Self-assembling flexible 2D carbide MXene film with tunable integrated electron migration and group relaxation toward energy storage and green EMI shielding. *Carbon* **2020**, *157*, 80−89.

(7) Cao, M. S.; Shu, J. C.; Wang, X. X.; Wang, X.; Zhang, M.; Yang, H. J.; Fang, X. Y.; Yuan, J. Electronic structure and electromagnetic properties for 2D electromagnetic functional materials in gigahertz frequency. *Ann. Phys.* **2019**, *531*, 1800390.

(8) Cui, X.; Liu, W.; Gu, W.; Liang, X.; Ji, G. Two-dimensional MoS2 modified using CoFe2O4 nanoparticles with enhanced microwave response in the X and Ku band. *Inorg. Chem. Front.* **2019**, *6*, 590−597.

(9) Chen, S.; Zhao, C.; Li, Y.; Huang, H.; Lu, S.; Zhang, H.; Wen, S. Broadband optical and microwave nonlinear response in topological insulator. *Opt. Mater. Express* **2014**, *4*, 587−596.

(10) Anju; Yadav, R. S.; Pötschke, P.; Pionteck, J.; Krause, B.; Kuřitka, I.; Vilcakova, J.; Skoda, D.; Urbánek, P.; Machovsky, M.; Masař, M.; Urbánek, M.; Jurca, M.; Kalina, L.; Havlica, J. High-Performance, Lightweight, and Flexible Thermoplastic Polyurethane Nanocomposites with Zn2+-Substituted CoFe2O4 Nanoparticles and Reduced Graphene Oxide as Shielding Materials against Electromagnetic Pollution. *ACS Omega* **2021**, *6*, 28098−28118.

(11) Guan, G.; Gao, G.; Xiang, J.; Yang, J.; Gong, L.; Chen, X.; Zhang, Y.; Zhang, K.; Meng, X. CoFe2/BaTiO3 hybrid nanofibers for microwave absorption. *ACS Appl. Nano Mater.* **2020**, *3*, 8424−8437.

(12) Li, Y.; Gao, T.; Zhang, W.; Hu, H.; Rong, H.; Zhang, X. Fe@CN x nanocapsules for microwave absorption at gigahertz frequency. *ACS Appl. Nano Mater.* **2019**, *2*, 3648−3653.

(13) Ohlan, A.; Singh, K.; Chandra, A.; Dhawan, S. K. Microwave absorption behavior of core− shell structured poly (3, 4-ethylenedioxy thiophene)− barium ferrite nanocomposites. *ACS Appl. Mater. Interfaces* **2010**, *2*, 927−933.

(14) Dhakate, S. R.; Subhedar, K. M.; Singh, B. P. Polymer nanocomposite foam filled with carbon nanomaterials as an efficient electromagnetic interference shielding material. *RSC Adv.* **2015**, *5*, 43036−43057.

(15) Phasuksom, K.; Prissanaroon-Ouajai, W.; Sirivat, A. A highly responsive methanol sensor based on graphene oxide/polyindole composites. *RSC Adv.* **2020**, *10*, 15206−15220.

(16) Faraz, M.; Shakir, M.; Khare, N. Highly sensitive and selective detection of picric acid using a one pot biomolecule inspired polyindole/CdS nanocomposite. *New J. Chem.* **2017**, *41*, 5784−5793.

(17) Anjitha, T.; Anilkumar, T.; Mathew, G.; Ramesan, M. T. Zinc ferrite@ polyindole nanocomposites: Synthesis, characterization and gas sensing applications. *Polym. Compos.* **2019**, *40*, 2802−2811.

(18) Rajasudha, G.; Rajeswari, D.; Lavanya, B.; Saraswathi, R.; Annapoorni, S.; Mehra, N. C. Colloidal dispersions of polyindole. *Colloid Polym. Sci.* **2005**, *283*, 575−582.

(19) Koiry, S. P.; Saxena, V.; Sutar, D.; Bhattacharya, S.; Aswal, D. K.; Gupta, S. K.; Yakhmi, J. V. Interfacial synthesis of long polyindole fibers. *J. Appl. Polym. Sci.* **2007**, *103*, 595−599.

(20) Phasuksom, K.; Sirivat, A. Synthesis of nano-sized polyindole via emulsion polymerization and doping. *Synth. Met.* **2016**, *219*, 142−153.

(21) Hoshina, Y.; Zaragoza-Contreras, E. A.; Farnood, R.; Kobayashi, T. Nanosized polypyrrole affected by surfactant agitation for emulsion polymerization. *Polym. Bull.* **2012**, *68*, 1689−1705.

(22) Peymanfar, R.; Mohammadi, A.; Javanshir, S. Preparation of graphite-like carbon nitride/polythiophene nanocomposite and investigation of its optical and microwave absorbing characteristics. *Compos. Commun.* **2020**, *21*, 100421.

(23) Nautiyal, A.; Ren, M. Q. T.; Huang, T.-S.; Zhang, X.; Cook, J.; Bozack, M. J.; Farag, R. High-performance engineered conducting polymer film towards antimicrobial/anticorrosion applications. *Eng. Sci.* **2018**, *4*, 70−78.

(24) Li, X.; Zhao, W.; Yin, R.; Huang, X.; Qian, L. A highly porous polyaniline-graphene composite used for electrochemical supercapacitors. *Eng. Sci.* **2018**, *3*, 89−95.

(25) Lou, C.; Jing, T.; Zhou, J.; Tian, J.; Zheng, Y.; Wang, C.; Zhao, Z.; Lin, J.; Liu, H.; Zhao, C.; Guo, Z. Laccase immobilized polyaniline/magnetic graphene composite electrode for detecting hydroquinone. *Int. J. Biol. Macromol.* **2020**, *149*, 1130−1138.

(26) Li, L.; Liu, S.; Lu, L. Synthesis and significantly enhanced microwave absorption properties of cobalt ferrite hollow microspheres with protrusions/polythiophene composites. *J. Alloys Compd.* **2017**, *722*, 158−165.

(27) Hu, Q.; Zhou, N.; Gong, K.; Liu, H.; Liu, Q.; Sun, D.; Wang, Q.; Shao, Q.; Liu, H.; Qiu, B.; Guo, Z. Intracellular polymer substances induced conductive polyaniline for improved methane production from anaerobic wastewater treatment. *ACS Sustainable Chem. Eng.* **2019**, *7*, 5912−5920.

(28) Wu, K.; Li, J.; Zhang, C. Zinc ferrite based gas sensors: A review. *Ceram. Interfaces* **2019**, *45*, 11143−11157.
(29) Hirosawa, F.; Iwasaki, T.; Watano, S. Synthesis and magnetic induction heating properties of Gd-substituted Mg−Zn ferrite nanoparticles. *Appl. Nanosci.* **2017**, *7*, 209−214.
(30) Tripathy, A.; Nine, M. J.; Silva, F. S. Biosensing platform on ferrite magnetic nanoparticle: Synthesis, functionalization, mechanism and applications. *Adv. Colloid Interface Sci.* **2021**, *290*, 102380.
(31) Chavan, V.; Thekkethil, V.; Pandey, A. K.; Iqbal, M.; Huskens, J.; Meena, S. S.; Goswami, A.; Verboom, W. Assembled diglycolamide for f-element ions sequestration at high acidity. *React. Funct. Polym.* **2014**, *74*, 52−57.
(32) Belaiche, Y.; Minaoui, K.; Ouadou, M.; Elansary, M.; Ahmani Ferdi, C. New nanosized (Gd3+, Sm3+) co-doped zinc ferrite: Structural, magnetic and first-principles study. *Phys. B* **2021**, *619*, 413262.
(33) Ghosh, R.; Pradhan, L.; Devi, Y. P.; Meena, S. S.; Tewari, R.; Kumar, A.; Sharma, S.; Gajbhiye, N. S.; Vatsa, R. K.; Pandey, B. N.; Ningthoujam, R. S. Induction heating studies of Fe3O4 magnetic nanoparticles capped with oleic acid and polyethylene glycol for hyperthermia. *J. Mater. Chem.* **2011**, *21*, 13388−13398.
(34) Li, B.; Weng, X.; Wu, G.; Zhang, Y.; Lv, X.; Gu, G. Synthesis of Fe 3 O 4 /polypyrrole/polyaniline nanocomposites by in-situ method and their electromagnetic absorbing properties. *J. Saudi Chem. Soc.* **2017**, *21*, 466−472.
(35) Kong, J.; Liu, J.; Wang, F.; Luan, L.; Itoh, M.; Machida, K.-i. Electromagnetic wave absorption properties of Fe3O4 octahedral nanocrystallines in gigahertz range. *Appl. Phys. A* **2011**, *105*, 351−354.
(36) Liu, Z.; Xing, H.; Wang, L.; Tan, D.; Gan, Y.; Ji, X.; Xu, G. Facial Synthesis of Zn-Doped Fe3O4 with Enhanced Electromagnetic Wave Absorption Performance in S and C Bands. *Nano* **2016**, *11*, 1650091.
(37) Xing, H.; Liu, Y.; Liu, Z.; Wang, H.; Jia, H. Structure and Microwave Absorption Properties of Polyaniline/Zn Ferrite Composites. *Nano* **2018**, *13*, 1850105.
(38) Zhu, W.; Wang, L.; Zhao, R.; Ren, J.; Lu, G.; Wang, Y. Electromagnetic and microwave-absorbing properties of magnetic nickel ferrite nanocrystals. *Nanoscale* **2011**, *3*, 2862−2864.
(39) Gu, X.; Zhu, W.; Jia, C.; Zhao, R.; Schmidt, W.; Wang, Y. Synthesis and microwave absorbing properties of highly ordered mesoporous crystalline NiFe2O4. *Chem. Commun.* **2011**, *47*, 5337−5339.
(40) Yan, J.; Huang, Y.; Chen, X.; Wei, C. Conducting polymers-NiFe2O4 coated on reduced graphene oxide sheets as electromagnetic (EM) wave absorption materials. *Synth. Met.* **2016**, *221*, 291−298.
(41) Wang, C.; Shen, Y.; Wang, X.; Zhang, H.; Xie, A. Synthesis of novel NiZn-ferrite/Polyaniline nanocomposites and their microwave absorption properties. *Mater. Sci. Semicond. Process.* **2013**, *16*, 77−82.
(42) Ting, T.; Yu, R. P.; Jau, Y. Synthesis and microwave absorption characteristics of polyaniline/NiZn ferrite composites in 2−40 GHz. *Mater. Chem. Phys.* **2011**, *126*, 364−368.
(43) Harris, V. G.; Geiler, A.; Chen, Y.; Yoon, S. D.; Wu, M.; Yang, A.; Chen, Z.; He, P.; Parimi, P. V.; Zuo, X.; Patton, C. E.; Abe, M.; Acher, O.; Vittoria, C. Recent advances in processing and applications of microwave ferrites. *J. Magn. Magn. Mater.* **2009**, *321*, 2035−2047.
(44) Verma, V.; Kapil, J.; Singh, N. Structural, magnetic properties of soft and hard ferrites and their EMI shielding application in X-band frequency range. *Int. J. Eng. Res.* **2014**, *3*, 557−560.
(45) Yang, C.; Li, H.; Xiong, D.; Cao, Z. Hollow polyaniline/Fe3O4 microsphere composites: Preparation, characterization, and applications in microwave absorption. *React. Funct. Polym.* **2009**, *69*, 137−144.
(46) Gandhi, N.; Singh, K.; Ohlan, A.; Singh, D. P.; Dhawan, S. K. Thermal, dielectric and microwave absorption properties of polyaniline−CoFe2O4 nanocomposites. *Compos. Sci. Technol.* **2011**, *71*, 1754−1760.
(47) Li, Z.; Ye, M.; Han, A.; Du, H. Preparation, characterization and microwave absorption properties of NiFe 2 O 4 and its composites with conductive polymer. *J. Mater. Sci. Mater.* **2016**, *27*, 1031−1043.
(48) Džunuzović, A.; Ilić, N.; Petrović, M. V.; Bobić, J.; Stojadinović, B.; Dohčević-Mitrović, Z.; Stojanović, B. Structure and properties of Ni−Zn ferrite obtained by auto-combustion method. *J. Magn. Magn. Mater.* **2015**, *374*, 245−251.
(49) Limpanart, S.; Arunsawad, S.; Srikulkit, K. Effect of surfactant on conductivity of poly (pyrrole-co-formyl pyrrole) via emulsion polymerization. *J. Met., Mater. Miner.* **2014**, *24*, 2.
(50) Ramesan, M. Synthesis and characterization of magnetoelectric nanomaterial composed of Fe3O4 and polyindole. *Adv. Polym. Technol.* **2013**, *32*, 928.
(51) Goel, S.; Mazumdar, N. A.; Gupta, A. Fabrication of polyindene and polyindole nanostructures. *Appl. Surf. Sci.* **2010**, *256*, 4426−4433.
(52) Elsayed, A.; Eldin, M. M.; Elsyed, A.; Elazm, A. A.; Younes, E.; Motaweh, H. Synthesis and properties of polyaniline/ferrites nanocomposites. *Int. J. Electrochem. Sci.* **2011**, *6*, 206−221.
(53) Afkhami, A.; Bahiraei, A.; Madrakian, T. Application of nickel zinc ferrite/graphene nanocomposite as a modifier for fabrication of a sensitive electrochemical sensor for determination of omeprazole in real samples. *J. Colloid Interface Sci.* **2017**, *495*, 1−8.
(54) Yavuz, Ö.; Ram, M. K.; Aldissi, M.; Poddar, P.; Hariharan, S. Synthesis and the physical properties of MnZn ferrite and NiMnZn ferrite−polyaniline nanocomposite particles. *J. Mater. Chem.* **2005**, *15*, 810−817.
(55) Jacob, B. P.; Kumar, A.; Pant, R. P.; Singh, S.; Mohammed, E. M. Influence of preparation method on structural and magnetic properties of nickel ferrite nanoparticles. *Bull. Mater. Sci.* **2011**, *34*, 1345−1350.
(56) Joshi, L.; Prakash, R. One-pot synthesis of Polyindole−Au nanocomposite and its nanoscale electrical properties. *Mater. Lett.* **2011**, *65*, 3016−3019.
(57) Zhang, M.; Liu, Q.; Zi, Z.; Dai, Y.; Zhu, X.; Sun, Y.; Dai, J. Magnetic and microwave absorption properties of Ni1−x Zn x Fe2O4 nanocrystalline synthesized by sol-gel method. *Sci. China: Technol. Sci.* **2013**, *56*, 13−19.
(58) Cheng, H.-W.; Li, J.; Wong, S.; Zhong, C.-J. Assessment of aggregative growth of MnZn ferrite nanoparticles. *Nanoscale* **2016**, *8*, 19359−19367.
(59) Wang, Y.; Li, G.; Zhang, Y.; Li, L. Zinc Ferrite Nanoparticles: Unusual Growth Mechanism for Size-Dependent Properties. *ChemistrySelect* **2021**, *6*, 1862−1869.
(60) Wang, R.; Zhou, W.; Lin, K.; Jiang, F.; Wang, Z.; Xu, J.; Zhang, Y.; Liang, A.; Nie, G.; Duan, X. Highly efficient electrochemical energy storage of fluorinated nano-polyindoles with different morphology. *Electrochim. Acta* **2020**, *349*, 136410.
(61) Thadathil, A.; Ismail, Y. A.; Periyat, P. Ternary 3D reduced graphene oxide/Ni0.5Zn0.5Fe2O4/polyindole nanocomposite for supercapacitor electrode application. *RSC Adv.* **2021**, *11*, 35828−35841.
(62) Dutta, P.; Dey, P.; Nath, T. K. Effect of nanometric grain size on room temperature magnetoimpedance, magnetoresistance, and magnetic properties of La0.7Sr0.3MnO3 nanoparticles. *J. Appl. Phys.* **2007**, *102*, 073906.
(63) Ghosh, S.; Patel, P. C.; Gangopadhyay, D.; Sharma, P.; Singh, R. K.; Srivastava, P. C. Structural and Magnetic Studies of Thermally Treated NiFe 2 O 4 Nanoparticles. *Metall. Mater. Trans. A* **2017**, *48*, 6135−6141.
(64) Zhang, M.; Zi, Z.; Liu, Q.; Zhang, P.; Tang, X.; Yang, J.; Zhu, X.; Sun, Y.; Dai, J. Size effects on magnetic properties of prepared by sol-gel method. *Adv. Mater. Sci. Eng.* **2013**, *2013*, 609819.
(65) George, M.; Mary John, A.; Nair, S. S.; Joy, P. A.; Anantharaman, M. R. Finite size effects on the structural and magnetic properties of sol-gel synthesized NiFe2O4 powders. *J. Magn. Magn. Mater.* **2006**, *302*, 190−195.
(66) Muthusamy, A.; Jawahar, V.; Kannapiran, N.; Anand, S.; Meena, S. S.; Yusuf, S. M. Preparation, Electrical and Magnetic Properties of Poly(m-phenylenediamine)/ZnFe2O4 Nanocomposites. *J. Supercond. Novel Magn.* **2018**, *31*, 497−504.

https://doi.org/10.1021/acsomega.2c00824
ACS Omega 2022, 7, 11473−11490

(67) Hashim, M.; Kumar, S.; Shirsath, S. E.; Kotnala, R.; Shah, J.; Kumar, R. Synthesis and characterizations of Ni2+ substituted cobalt ferrite nanoparticles. *Mater. Chem. Phys.* **2013**, *139*, 364−374.
(68) Kagdi, A. R.; Solanki, N. P.; Carvalho, F. E.; Meena, S. S.; Bhatt, P.; Pullar, R. C.; Jotania, R. B. Influence of Mg substitution on structural, magnetic and dielectric properties of X-type barium zinc hexaferrites Ba2Zn2-xMgxFe28O46. *J. Alloys Compd.* **2018**, *741*, 377−391.
(69) Jing, X.; Shen, X.; Song, H.; Song, F. Magnetic and dielectric properties of barium ferrite fibers/poly(vinylidene fluoride) composite films. *J. Polym. Res.* **2011**, *18*, 2017−2021.
(70) Liu, X.; Liu, S.; Han, M.-G.; Zhao, L.; Deng, H.; Li, J.; Zhu, Y.; Krusin-Elbaum, L.; O'Brien, S. Magnetoelectricity in CoFe2O4 nanocrystal-P(VDF-HFP) thin films. *Nanoscale Res. Lett.* **2013**, *8*, 374.
(71) Muthusamy, A.; Arunkumar, M.; Kannapiran, N.; Meena, S. S.; Yusuf, S. M. Electrical and magnetic properties of poly(m-phenylenediamine)/NiFe2O4 nanocomposites. *J. Mater. Sci. Mater.* **2017**, *28*, 15754−15761.
(72) Hussain, S.; Anis-ur-Rehman, M.; Maqsood, A.; Awan, M. S. The effect of SiO2 addition on structural, magnetic and electrical properties of strontium hexa-ferrites. *J. Cryst. Growth* **2006**, *297*, 403−410.
(73) Kechrakos, D.; Trohidou, K. N. Magnetic properties of dipolar interacting single-domain particles. *Phys. Rev. B* **1998**, *58*, 12169.
(74) Vargas, J. M.; Nunes, W. C.; Socolovsky, L. M.; Knobel, M.; Zanchet, D. Effect of dipolar interaction observed in iron-based nanoparticles. *Phys. Rev. B* **2005**, *72*, 184428.
(75) Jiang, D.; Murugadoss, V.; Wang, Y.; Lin, J.; Ding, T.; Wang, Z.; Shao, Q.; Wang, C.; Liu, H.; Lu, N.; Wei, R.; Subramania, A.; Guo, Z. Electromagnetic Interference Shielding Polymers and Nanocomposites - A Review. *Polym. Rev.* **2019**, *59*, 280−337.
(76) Ding, D.; Wang, Y.; Li, X.; Qiang, R.; Xu, P.; Chu, W.; Han, X.; Du, Y. Rational design of core-shell Co@C microspheres for high-performance microwave absorption. *Carbon* **2017**, *111*, 722−732.
(77) Singh, K.; Ohlan, A.; Pham, V. H.; Balasubramaniyan, R.; Varshney, S.; Jang, J.; Hur, S. H.; Choi, W. M.; Kumar, M.; Dhawan, S. K.; Kong, B.-S.; Chung, J. S. Nanostructured graphene/Fe3O4 incorporated polyaniline as a high performance shield against electromagnetic pollution. *Nanoscale* **2013**, *5*, 2411−2420.
(78) Wang, Y.; Du, Y.; Xu, P.; Qiang, R.; Han, X. Recent advances in conjugated polymer-based microwave absorbing materials. *Polymers* **2017**, *9*, 29.
(79) Liu, P.; Huang, Y.; Yan, J.; Zhao, Y. Magnetic graphene@PANI@porous TiO2 ternary composites for high-performance electromagnetic wave absorption. *J. Mater. Chem. C* **2016**, *4*, 6362−6370.
(80) Chen, D.; Wang, G.-S.; He, S.; Liu, J.; Guo, L.; Cao, M.-S. Controllable fabrication of mono-dispersed RGO-hematite nanocomposites and their enhanced wave absorption properties. *J. Mater. Chem. A* **2013**, *1*, 5996−6003.
(81) Zhang, P.; Han, X.; Kang, L.; Qiang, R.; Liu, W.; Du, Y. Synthesis and characterization of polyaniline nanoparticles with enhanced microwave absorption. *RSC Adv.* **2013**, *3*, 12694−12701.
(82) Jaiswal, A.; Das, R.; Maity, T.; Poddar, P. Dielectric and spin relaxation behaviour in DyFeO3 nanocrystals. *J. Appl. Phys.* **2011**, *110*, 124301.
(83) Shen, G.; Mei, B.; Wu, H.; Wei, H.; Fang, X.; Xu, Y. Microwave electromagnetic and absorption properties of N-doped ordered mesoporous carbon decorated with ferrite nanoparticles. *J. Phys. Chem. C* **2017**, *121*, 3846−3853.
(84) Wan, G.; Yu, L.; Peng, X.; Wang, G.; Huang, X.; Zhao, H.; Qin, Y. Preparation and microwave absorption properties of uniform TiO2@C core-shell nanocrystals. *RSC Adv.* **2015**, *5*, 77443−77448.
(85) Zhao, B.; Shao, G.; Fan, B.; Xie, Y.; Wang, B.; Zhang, R. Solvothermal synthesis and electromagnetic absorption properties of pyramidal Ni superstructures. *J. Mater. Res.* **2014**, *29*, 1431−1439.
(86) Al-Saleh, M. H.; Saadeh, W. H.; Sundararaj, U. EMI shielding effectiveness of carbon based nanostructured polymeric materials: a comparative study. *Carbon* **2013**, *60*, 146−156.
(87) Nallabothula, H.; Bhattacharjee, Y.; Samantara, L.; Bose, S. Processing-mediated different states of dispersion of multiwalled carbon nanotubes in PDMS nanocomposites influence EMI shielding performance. *ACS Omega* **2019**, *4*, 1781−1790.
(88) Danlée, Y.; Bailly, C.; Huynen, I. Thin and flexible multilayer polymer composite structures for effective control of microwave electromagnetic absorption. *Compos. Sci. Technol.* **2014**, *100*, 182−188.

https://doi.org/10.1021/acsomega.2c00824
ACS Omega 2022, 7, 11473−11490